

# 13 Theoretical Description of ARPES: The One-Step Model

Ján Minár

Department Chemie, Physikalische Chemie

Ludwig-Maximilians-Universität München

New Technologies-Research Center

University of West Bohemia, Plzen

## Contents

<b>1</b>	<b>Introduction</b>	<b>2</b>
<b>2</b>	<b>Combination of the LSDA+DMFT with the KKR method</b>	<b>3</b>
2.1	LSDA+DMFT treatment of disordered alloys . . . . .	7
<b>3</b>	<b>One-step model of photoemission</b>	<b>9</b>
3.1	General theory of photoemission . . . . .	10
3.2	Fully relativistic one-step model of photoemission for alloys . . . . .	12
<b>4</b>	<b>LSDA+DMFT for calculations of spectroscopic properties</b>	<b>16</b>
4.1	Angle-integrated valence band photoemission: Fano effect . . . . .	16
4.2	ARPES: Correlation effects in transition-metals and their surfaces . . . . .	17
4.3	ARPES of disordered correlated alloys: $\text{Ni}_x\text{Pd}_{1-x}$ (001) . . . . .	23
<b>5</b>	<b>Angle resolved soft and hard X-ray photomission</b>	<b>24</b>
5.1	Photon momentum effects: Ag(001) . . . . .	26
5.2	Thermal effects and XPS limit . . . . .	29
<b>6</b>	<b>Summary</b>	<b>32</b>

# 1 Introduction

Angle resolved photoemission (ARPES) and bremsstrahlung isochromat spectroscopy (ARBIS) have developed over several decades into the experimental techniques for directly determining the electronic structure of any new material [1, 2]. These experimental techniques allow to measure the dispersion of occupied bands as well as unoccupied bands and therefore reveal the electronic structure around the Fermi level with a high amount of accuracy. In particular, in recent years many improvements on the experimental side have led to an increase of the resolution of ARPES down to the meV-regime. These improvements are primarily due to the use of synchrotron radiation, and laser sources, and to developments on the detector side (e.g. spin resolution). More details on the foundations of ARPES can be found in the lecture of M. Sing.

On the theory side, about 50 years ago photoemission theory appeared to be an intractable many-body problem [3–7]. The first and most simple version of a one-electron approximation for the photocurrent was given by Berglund and Spicer [8], the so called three-step model of photoemission. In the framework of this model the photoemission process is divided into three independent steps: the excitation of the photoelectron, its transport through the crystal and its escape into the vacuum. Self-energy corrections, which represent, among others, damping processes and energetic shifts in the quasi-particle spectrum, are completely neglected. This means that the initial and final states in the photoemission process are assumed to be Bloch-states with an infinite lifetime. It should be mentioned that the assumption of an infinite electron lifetime does not allow for transitions into evanescent bandgap states, e.g. states that decay exponentially into the solid. Similarly, the assumption of an infinite lifetime for the initial state does in practice not allow to calculate photoemission spectra that involve surface states. To overcome the deficiencies of the three-step model, a dynamic approach has been suggested first for the final state by Liebsch [9] and Spanjaard *et al.* [10]. Later-on multiple scattering effects were properly included for both initial and final states by Pendry and coworkers [11, 12] in order to treat self-energy corrections on an equal footing. Pendry's one-step approach to ARPES [11, 13] led to a numerically solvable scheme by replacing the retarded one-electron Green function for the initial state by the one-particle Green function determined within density functional theory (DFT) [14]. Within this scheme, electronic correlation effects are typically considered in photoemission theory making use in practice of the local (spin) density approximation (L(S)DA) [15, 16]. Life-time effects in the initial state are accounted for by an imaginary potential term  $V_{0i}$  which is added to the single-particle cell potential. The final state is constructed within the formalism for spin-polarized low-energy electron diffraction (SPLEED) as a so-called time-reversed SPLEED state [13, 17]. The finite imaginary part  $V_{0fi}$  effectively simulates the inelastic mean free path (IMFP). As a consequence the amplitude of the high-energy photoelectron state inside the solid can be neglected beyond a certain distance from the surface [11].

After the one-step model had been established in the seventies, it was extended in many aspects. For example, the quantitative analysis of spin-orbit induced dichroic phenomena was worked out by several groups [17–24]. Furthermore, the so called full-potential formulation of photoemission was developed in order to achieve an accurate description of spectroscopic data even

for complex surface systems [17, 23, 25]. The treatment of disordered systems was worked out by Durham *et al.* [26, 20]. Nowadays, the one-step model allows for photocurrent calculations for photon energies ranging from a few eV to more than 10 keV [27–34], for finite temperatures and for arbitrarily ordered [35] and disordered systems [36], and considering in addition strong correlation effects within the dynamical mean-field theory (DMFT) [37–42]. The aim of this lecture is to present these recent developments in the theory of photoemission. The main emphasis will be given to its LSDA+DMFT extension and to the relatively new techniques of soft- and hard x-ray angle resolved photoemission (HARPES).

The LSDA+DMFT implementation within the multiple-scattering Korringa-Kohn-Rostoker (KKR) method [37, 43] is reviewed in Sec. 2. In section 3.2, we briefly review the one-step model of photoemission. The second part of this lecture is devoted to calculations of angle-resolved photoemission within the one-step model including more or less all relevant spectroscopy issues like matrix elements and surface effects. Recent technical developments allow one to perform calculations for ordered as well as for chemically disordered systems including electronic correlation effects. This topic is presented in Sec. 4. Finally, several aspects of soft and hard x-ray photoemission, which are relatively new experimental methods, are discussed in Sec. 5.

## 2 Combination of the LSDA+DMFT with the KKR method

In the following section we shortly review a fully self-consistent (with respect to charge density and self-energy) LSDA+DMFT implementation within the full-potential fully relativistic multiple scattering Korringa Kohn Rostoker method [37]. This method is used to solve the multiple scattering formalism for semi-infinite solids which in turn is a basis of the one-step model of photoemission as presented in next section. The KKR offers a number of advantages compared to other band structure methods due to the fact that the KKR represents the electronic structure by the corresponding single-particle Green's function (For a recent review of the KKR method see [44] and references therein). This allows one to combine the KKR method with the DMFT straightforwardly. Another important consequence is the possible use of the Dyson equation which relates the Green's function of a perturbed system with the Green's function of the corresponding unperturbed reference system. Using the Dyson equation allows in particular to calculate the properties of low dimensional systems like, e.g., semi-infinite 2D-surfaces, nanostructures or embedded 3D- or 2D- systems without using an artificial super cell construction. Finally, the KKR Green's function method allows one to deal with substitutional disordered alloys in combination with the coherent potential approximation (CPA) [45].

The central idea of the KKR-based implementation of the LSDA+DMFT is to account for the general non-local, site-diagonal, complex and energy-dependent self-energy  $\Sigma^{\text{DMFT}}$  already when calculating the basis functions, i.e., when solving the single-site Schrödinger (or Dirac) equation. This allows one to exploit directly all advantageous features of the KKR Green's function method when performing LSDA+DMFT calculations and consequently to account for correlation effects for a wide range of systems.

There are nowadays various approaches available to combine the LSDA with the DMFT method [46,47]. In contrast to the KKR-scheme, the corresponding LSDA problem is in general solved variationally using a given basis set (e.g. LMTO) as a first step. The corresponding local Green's function is determined by the spectral representation of the Kohn-Sham Hamiltonian. Solving subsequently the DMFT problem, the resulting local self-energy  $\Sigma^{\text{DMFT}}$  and local Green's function can in turn be used to calculate a new charge density and an effective LSDA potential. However, in order to combine coherently the LSDA with the DMFT method (in the spirit of spectral density functional theory [48]) one has to solve self-consistently the following Dyson equation

$$G(\vec{r}, \vec{r}', E) = G_0(\vec{r}, \vec{r}', E) + \int d^3r'' \int d^3r''' G_0(\vec{r}, \vec{r}'', E) \left( V_{\text{eff}}(\vec{r}'') \delta(\vec{r}'' - \vec{r}''') + \Sigma(\vec{r}'', \vec{r}''', E) \right) G(\vec{r}''', \vec{r}', E), \quad (1)$$

where  $G_0(\vec{r}, \vec{r}'', E)$  is the free electron Green's function. The potential  $V_{\text{eff}}(\vec{r})$  denotes the (effective) potential. Within the relativistic version of spin DFT used here this is usually defined as  $V_{\text{eff}}(\vec{r}) = [\bar{V}_{\text{eff}}(\vec{r}) + \beta \boldsymbol{\sigma} \mathbf{B}_{\text{eff}}(\vec{r})]$  where  $\bar{V}_{\text{eff}}(\vec{r})$  denotes the spin-independent potential, and  $\mathbf{B}_{\text{eff}}(\vec{r})$  is the magnetic field [49]. Correspondingly, the matrices  $\beta$  and  $\alpha_k$  used below are the standard Dirac matrices with  $\beta = \sigma_z \otimes 1_2$  and  $\alpha_k = \sigma_x \otimes \sigma_k$  ( $k = x, y, z$ ) in terms of the  $2 \times 2$  Pauli-matrices  $\sigma_k$ .

A very efficient way of solving Eq. (1) is offered by the multiple scattering KKR method. Having decomposed the system into atomic regions (Wigner-Seitz-cells) and considering that  $\Sigma^{\text{DMFT}}$  is an on-site quantity, the equation can be solved using the standard KKR formalism. This implies that one first has to solve the single-site scattering problem to obtain the wave function  $\Psi(\vec{r})$  and the corresponding single-site scattering  $t$ -matrix inside an atomic cell. In the relativistic spin density functional theory [50,51] the corresponding single-site Dirac equation reads

$$\left[ \frac{\hbar}{i} c \vec{\alpha} \cdot \vec{\nabla} + \beta m c^2 + V_{\text{eff}}(\vec{r}) + \int d^3r' \Sigma(\vec{r}, \vec{r}', E) \right] \Psi(\vec{r}) = E \Psi(\vec{r}). \quad (2)$$

Here, the  $\Psi(\vec{r})$  are energy-dependent four-component spinor functions for energy  $E$ . To be able to solve Eq. (2) one makes the following ansatz for the wave function  $\Psi = \sum_{\Lambda} \Psi_{\Lambda}$ , with the combined relativistic quantum number  $\Lambda = (\kappa, \mu)$ , where  $\kappa$  and  $\mu$  are the spin-orbit and magnetic quantum numbers, respectively. In addition, in the spirit of the DMFT one has to project  $\Sigma(\vec{r}, \vec{r}', E)$  onto the localized set of orbitals  $\phi_{\Lambda}^n(\vec{r})$ . The corresponding matrix  $\Sigma_{\Lambda\Lambda'}(E)$  is obtained as an output from the DMFT solver. In practice,  $\Sigma_{\Lambda\Lambda'}(E)$  is used only for correlated  $d$ - or  $f$ -orbitals. It is worth noting that even in the case of the spherical muffin-tin or atomic-sphere approximation to the potential, the full-potential-like coupled Eqs. (2) have to be solved. This implies that the full-potential version of the KKR has to be used. After having solved the set of coupled equations for the wave functions  $\Psi(\vec{r})$  one gets the corresponding single-site  $t$  matrix by standard matching to the Hankel and Bessel functions as free-electron solutions. When solving the single-site problem, obviously the entire complexity of the underlying complex non-local

potential within LSDA+DMFT is accounted for. Accordingly, the resulting regular and irregular scattering wave functions  $Z_\Lambda(\vec{r}, E)$  and  $J_\Lambda(\vec{r}, E)$  as well as the corresponding single-site  $t$ -matrix carry all information of the underlying LSDA+DMFT Hamiltonian. This means that in contrast to other LSDA+DMFT implementations, the effect of the self-energy is also reflected in the wave functions  $\Psi$ . This becomes important, for example, in a total energy calculation and for the photoemission matrix elements (see Sec. 3.2).

With the single-site  $t$  matrix available the next step of the KKR calculation is to solve the multiple scattering problem. This task can be done by using the scattering path operator  $\tau$  [52] and it is independent from the DMFT. For a finite system this can be done straightforwardly by inverting the so called KKR-matrix,  $\underline{\underline{\tau}}(E) = [\underline{\underline{t}}(E)^{-1} - \underline{\underline{G}}_0(E)]^{-1}$  with the double underline indicating matrices with respect to site and spin-angular ( $\Lambda$ ) character. Dealing with a three-dimensional periodic system this equation can also be solved exactly by Fourier transformation. As a result the retarded site-diagonal Green's function  $G(\vec{r}, \vec{r}', E)$  can be written as [53, 45]

$$\begin{aligned} G(\vec{r}, \vec{r}', E) &= \sum_{\Lambda, \Lambda'} Z_\Lambda(\vec{r}, E) \tau_{\Lambda, \Lambda'}^{nn}(E) Z_{\Lambda'}^\times(\vec{r}', E) \\ &- \sum_{\Lambda} \{ Z_\Lambda(\vec{r}, E) J_\Lambda^\times(\vec{r}', E) \Theta(\vec{r}' - \vec{r}) \\ &+ J_\Lambda(\vec{r}, E) Z_\Lambda^\times(\vec{r}', E) \Theta(\vec{r} - \vec{r}') \}, \end{aligned} \quad (3)$$

where  $\vec{r}$  ( $\vec{r}'$ ) lies in the atomic cell  $n$  representing cell-centered coordinates and  $\times$  indicates a so-called left-hand side solution [54]. With the Green's function  $G(\vec{r}, \vec{r}', E)$  available all properties of interest, e.g., the charge density, can be calculated straightforwardly and in this way the calculated Green's function  $G$  includes all effects of the self-energy  $\Sigma^{\text{DMFT}}$ .

The definition of the Green's function and the expressions given above are not restricted to real energies  $E$  but also hold for arbitrary complex energies  $z$ . The fact that  $G(\vec{r}, \vec{r}', E)$  is analytical [55] allows, in particular, to perform the energy integration for the charge density on a contour in the complex energy plane [56] with typically around 30 energy mesh points. On the other hand the self-energy  $\Sigma^{\text{DMFT}}$  is often calculated for a mesh of Matsubara frequencies. This implies that it is necessary to use analytical continuation techniques to transform  $\Sigma^{\text{DMFT}}$  from Matsubara frequencies  $\omega$  onto the KKR complex energy contour. It is worth noting that in general  $\Sigma^{\text{DMFT}}$  is not Hermitian and for low-symmetry systems one has to consider right- and left-handed solutions of (2) when constructing the Green's function  $G(\vec{r}, \vec{r}', E)$  [54].

In order to construct the bath Green's function needed as the input of the DMFT solver, the localized Green's function is calculated by projecting the Green's function given by Eq. (3) onto the correlated atomic orbitals  $\phi_\Lambda(\vec{r})$

$$G_{\Lambda\Lambda'}(E) = \int d^3r \int d^3r' \phi_\Lambda(\vec{r}) G(\vec{r}, \vec{r}', E) \phi_{\Lambda'}(\vec{r}'). \quad (4)$$

A natural choice for the projection functions  $\phi_\Lambda(\vec{r})$  are the regular single-site solutions of the Kohn-Sham-Dirac equations that are normalized to 1 and also are used to represent the self energy  $\Sigma$ . For transition-metal systems, only the  $d$ - $d$  sub-block of the  $\underline{\underline{G}}^{nn}(E)$  is considered,

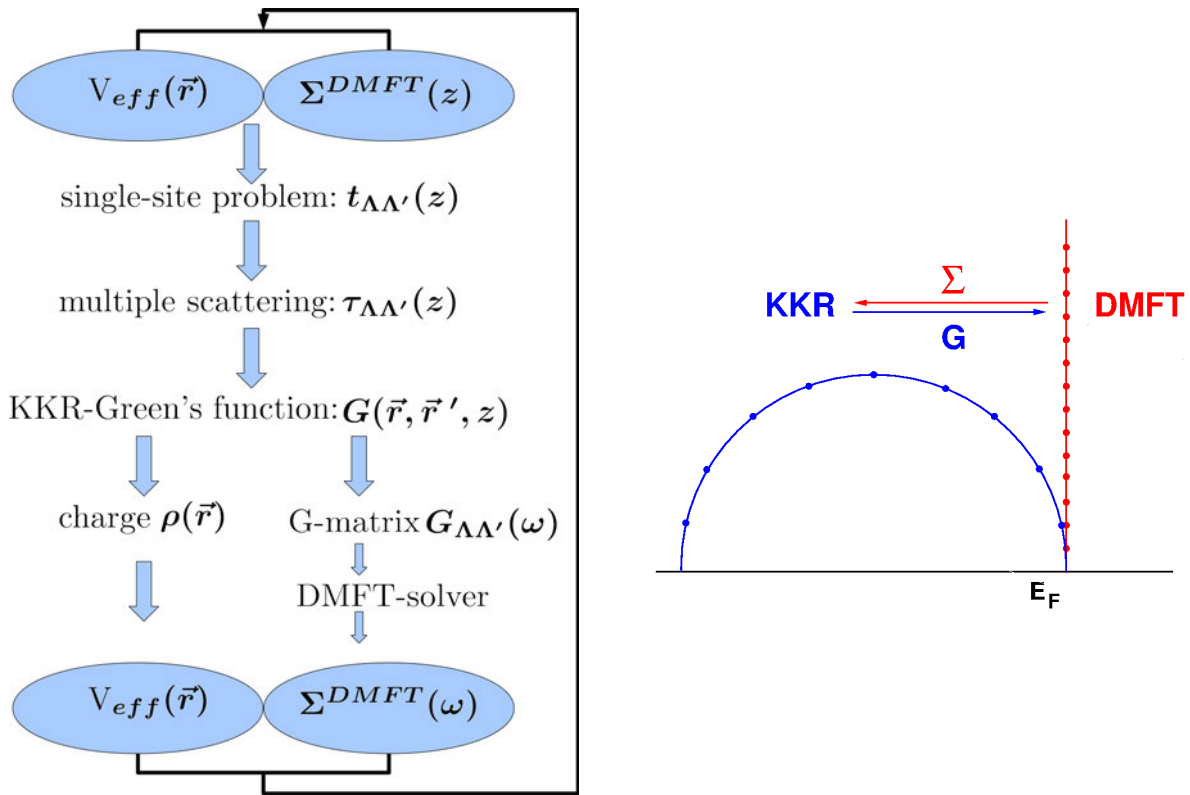


**Fig. 1:** *Left: Schematic overview of the KKR-based LSDA+DMFT scheme. Right: Illustration of the energy paths involved. The blue semicircle is the complex energy path (with complex energies  $z$ ) used by KKR to calculate the charge density. After the bath Green's function  $G$  is obtained, it is analytically continued onto the imaginary axis (red) to calculate the self-energy  $\Sigma^{DMFT}$  via the DMFT impurity solver. The latter is analytically extrapolated back to the semicircle. Figure taken from [43].*

using  $\phi_{\Lambda}(\vec{r})$  wave functions with  $l = 2$ . In principle, the choice of the  $\phi_{\Lambda}(\vec{r})$  is arbitrary as long as  $\phi_{\Lambda}(\vec{r})$  is a complete set of functions. This implies that a localized basis set is calculated at a given reference energy  $E_{\text{ref}}$  (set to be the center of gravity of the occupied  $d$ - or  $f$ -band) with the magnetic field set to zero in the relativistic case. In the full-potential case couplings to the other  $l$ -channels as a consequence of crystal symmetry have to be suppressed.

A flow diagram describing the resulting KKR-based self-consistent LSDA+DMFT scheme is presented in Fig. 1. Eq. (2) provides the set of regular ( $Z$ ) and irregular ( $J$ ) solutions of the single-site problem accounting for the LSDA potential as well as the DMFT self-energy  $\Sigma$ . Together with the  $t$ -matrix and the scattering-path operator  $\tau$  the KKR Green's function is constructed from Eq. (3). To solve the many-body problem, the projected Green's function matrix is constructed according to Eq. (4). The LSDA Green's function  $G_{\Lambda\Lambda'}(E)$  is calculated on the complex contour which encloses the valence band one-electron energy poles. The Padé analytical continuation scheme is used to map the complex local Green's function  $G_{\Lambda\Lambda'}(E)$  onto the set of Matsubara frequencies or the real axis, which is used when dealing with the many-

body problem. In the current fully relativistic implementation, the perturbative SPTF (spin-polarized  $T$ -matrix + FLEX) [57] as well as  $T = 0$  K spin-polarized  $T$ -matrix [58] solvers of the DMFT problem are used. In fact any DMFT solver could be included which supplies the self-energy  $\Sigma(E)$  when solving of the many-body problem. The Padé analytical continuation is used once more to map the self-energy from the Matsubara axis back onto the complex plane, where the new KKR Green's function is calculated. As was described in the previous sections, the key role is played by the scattering path operator  $\tau_{AA'}^{mn}(E)$ , which allows us to calculate the charge in each SCF iteration and the new potentials that are used to generate the new single particle Green's function.

Finally, the double-counting corrections  $H_{DC}$  have to be considered. This problem is definitely one of the main challenges towards first-principles calculations within LSDA+DMFT. Until now various schemes for double-counting correction have been suggested [47]. The simplest choice, i.e., the idea of the static LSDA+ $U$  scheme has been used here. We apply the double-counting corrections to the self-energy when solving the many-body problem. First of all we remove the static part of the self-energy coming from the SPTF solver and add the mean-field (AMF) LSDA+ $U$  like static part [59]. In the case of pure transition metals, as well as their metallic compounds and alloys, the so-called AMF double-counting correction seems to be most appropriate [59, 38, 40, 60]. It is worth noting here that currently an exact analytical equation for the double-counting correction is not known. Alternatively, it might be possible to get an exact solution of the double-counting problem on the level of the GW+DMFT scheme [61]. Therefore, it is important to perform direct comparisons, for example, to ARPES experiments as a stringent test for the choice of the optimal  $H_{DC}$ . However, to be able to make a decision between various suggestions for  $H_{DC}$  it is helpful not only to calculate the bare spectral function, i.e.  $\text{Im} G$ , but also to perform a complete calculation of photoemission spectra (for example with the one-step model of photoemission, see Sec. 3.2). In fact, using the one-step model of photoemission, one can clearly see that the AMF  $H_{DC}$  is an appropriate choice at least for transition-metal systems [38, 40, 60].

## 2.1 LSDA+DMFT treatment of disordered alloys

It is an outstanding feature of the KKR method that it supplies the one-electron Green's function of the considered system directly without relying on Bloch's theorem. Because of this property, the KKR Green's function method allows one to deal with substitutional disorder including both diluted impurities and concentrated alloys in the framework of the CPA [62, 63]. Within this approach (KKR-CPA) the propagation of an electron in an alloy is regarded as a succession of elementary scattering processes due to random atomic scatterers, with an average taken over all configurations of the atoms. This problem can be solved assuming that a given scattering center is embedded in an effective medium whose choice is open and can be determined in a self-consistent way. The physical condition corresponding to the CPA is simply that a single scatterer embedded in the effective CPA medium should produce no further scattering on the average as illustrated by Fig. 2.

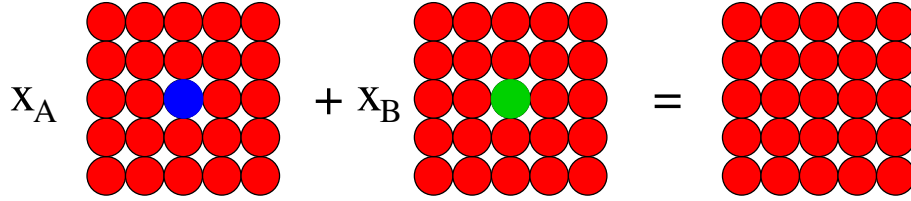


**Fig. 2:** The major ideas of the CPA: The configurational average over all configurations of a disordered alloy  $A_x B_{1-x}$  is represented by an auxiliary CPA medium. Embedding of an A or B atom should not give rise to additional scattering with respect to the CPA medium.

A similar philosophy is applied also when dealing with many-body problems for crystals in the framework of DMFT. Thus it is rather straightforward to combine the DMFT and KKR-CPA method as both schemes are used on a single-site level, i.e., any correlation in the occupation (e.g. short range order) is ignored and the DMFT self-energy  $\Sigma$  is taken to be on-site only. In fact, the combination of the KKR-CPA for disordered alloys and the DMFT scheme is based on the same arguments as used by Drchal *et al.* [64] when combining the LMTO Green's function method for alloys [65] with the DMFT.

The combination of the CPA and LSDA+DMFT turned out to be a rather powerful technique for calculating electronic structure properties of substitutionally disordered correlated materials [37, 59, 66, 36]. As mentioned, within the CPA the configurationally averaged properties of a disordered alloy are represented by a hypothetical ordered CPA-medium, which in turn may be described by a corresponding site-diagonal scattering path operator  $\tau^{\text{CPA}}$ , which in turn is closely connected with the electronic Green's function. For example for a binary system  $A_x B_{1-x}$  composed of components A and B with relative concentrations  $x$  and  $1 - x$  the corresponding single-site  $t$ -matrix  $t^{\text{CPA}}$  and the multiple scattering path operator  $\tau^{\text{CPA}}$  are determined by the so called CPA-condition:

$$x\tau^{\text{A}} + (1 - x)\tau^{\text{B}} = \tau^{\text{CPA}}. \quad (5)$$

The CPA equation represents the requirement that substitutionally embedding an atom (of type A or B) into the CPA medium should not cause additional scattering. The scattering properties of an A atom embedded in the CPA medium are represented by the site-diagonal component-projected scattering path operator  $\tau^{\text{A}}$  (angular momentum index omitted here)

$$\tau^{\text{A}} = \tau^{\text{CPA}} \left[ 1 + (t_{\text{A}}^{-1} - t_{\text{CPA}}^{-1}) \tau^{\text{CPA}} \right]^{-1} = \tau^{\text{CPA}} \mathcal{D}^{\text{A}}, \quad (6)$$

where  $t_{\text{A}}$  and  $t_{\text{CPA}}$  are the single-site matrices of the A component and of the CPA effective medium; the factor  $\mathcal{D}^{\text{A}} = [1 + (t_{\text{A}}^{-1} - \tau_{\text{CPA}}^{-1})]^{-1}$  in Eq. (6) is called the CPA-projector. A corresponding equation holds also for the B component in the CPA medium. The coupled set of equations for  $\tau^{\text{CPA}}$  and  $t_{\text{CPA}}$  has to be solved iteratively within the CPA cycle. For example when a binary system  $A_x B_{1-x}$  composed of components A and B with relative concentrations  $x_{\text{A}} = x$  and  $x_{\text{B}} = (1 - x)$  is considered, the above equation represents the requirement that embedding substitutionally an atom (of type A or B) into the CPA medium should not cause additional scattering.

The above scheme can straightforwardly be extended to include many-body correlation effects for disordered alloys [37]. Within the KKR approach the local multi-orbital and energy dependent self-energies ( $\Sigma_A^{DMFT}(E)$  and  $\Sigma_B^{DMFT}(E)$ ) are directly included into the single-site matrices  $t_A$  and  $t_B$ , respectively when solving the corresponding Dirac equation (2). Consequently, all the relevant physical quantities connected with the Green's function, for example the charge density, contain the electronic correlations beyond the LSDA scheme.

### 3 One-step model of photoemission

Spectroscopy is an extremely important experimental tool providing information on the electronic structure of the probed system that has to be seen as a stringent benchmark for the success of any electron structure theory. Photoemission spectroscopy (PES) or its inverse – the Bremsstrahlung isochromate spectroscopy (BIS) – in their angle-integrated form should reflect the density of states (DOS) rather directly, in particular in the high photon-energy regime (XPS). For that reason it is quite common to check the DMFT-based calculations by comparing the calculated DOS directly to the PES spectra (see the reviews [67, 46, 47] for example).

However, this approach ignores the influence of the specific PES matrix elements that in general will introduce an element- and energy-dependent weight to the partial DOS. In ARPES, the situation is even more severe as the surface as well as dipole selection rules may have a pronounced impact on the spectra [68] demanding a coherent description on the basis of the one-step model of photoemission [17]. To achieve a reliable interpretation of experiments it is inevitable to deal with so-called matrix-element effects that considerably modify the raw spectrum. In particular, the wave-vector and energy dependence of the transition-matrix elements has to be accounted for. These issues are known to be important and cannot be neglected. They arise from strong multiple-scattering processes in the final PES state that dominate the electron dynamics in the low-energy regime of typically 1-200 eV [13]. The transition-matrix elements also include the effects of selection rules which are not accounted for in the raw spectrum. Loosely speaking, it can be said that the main task of a theory of photoemission is to close the gap between the raw spectrum obtained by LSDA+DMFT electronic-structure calculations and the experiment. The most successful theoretical approach concerning this is the one-step model of photoemission as originally proposed by Pendry and co-workers [11–13]. In the following a short overview will be given on the recent extensions of this model which are connected with correlation effects and disordered alloys.

The main idea of the one-step model is to describe the actual excitation process, the transport of the photoelectron to the crystal surface as well as the escape into the vacuum [8] as a single quantum-mechanically coherent process including all multiple-scattering events. Within this model self-energy corrections, which give rise to damping in the quasi-particle spectrum, are properly included in both the initial and the final states. This, for example, allows for transitions into evanescent band gap states decaying exponentially into the solid. Similarly, the assumption of a finite lifetime for the initial states gives the opportunity to calculate photoemission intensities from surface states and resonances. Treating the initial and final states within the

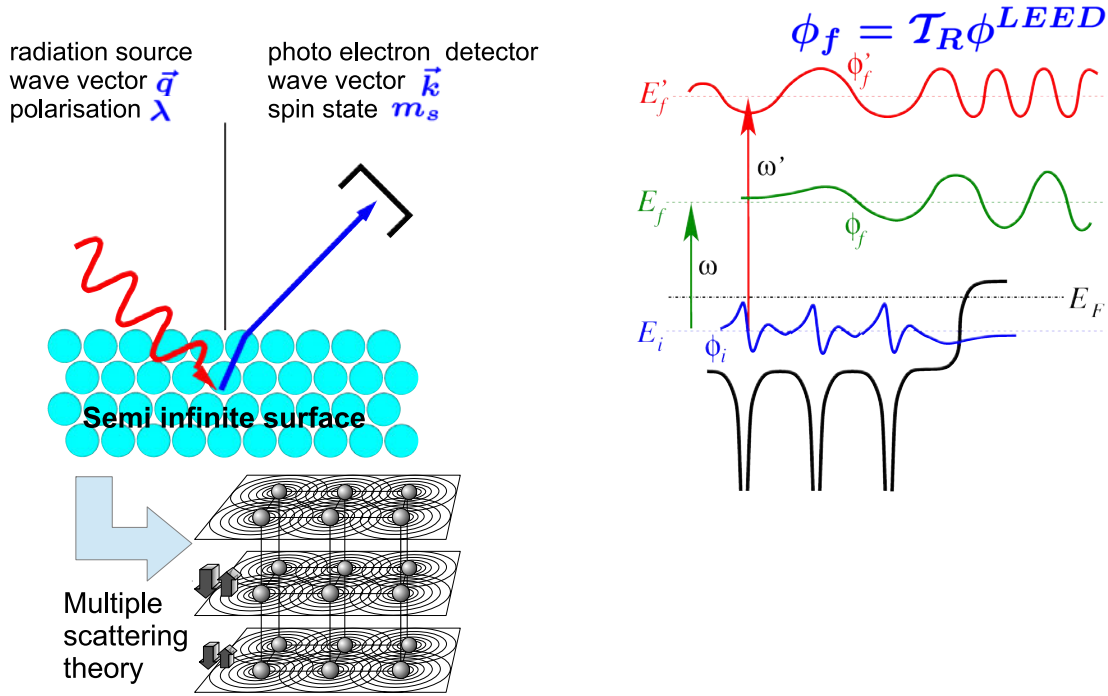


**Fig. 3:** *Left: Schematic overview of the one-step model of photoemission. The whole photoemission process is solved within the multiple scattering theory for a semi-infinite surface. Right: Electron from initial state  $\phi_i$  at energy  $E_i$  is excited to the final state  $\phi_f$  (time-reversed SPLEED) which decays into the solid due to the inelastic processes (modeled by imaginary part of potential). By increasing the inelastic mean free path of the time-reversed SPLEED state ( $E'_f$ ) the photoemission process becomes more bulk sensitive (See Sec. 5).*

fully relativistic layer version of the KKR [69, 70], it is a straightforward task to describe the photoemission from complex layered structures like thin films and multilayers. Furthermore, the surface described by a barrier potential can be easily included into the multiple-scattering formalism as an additional layer. A realistic surface barrier model that shows the correct asymptotic behavior has been introduced, for example, by Rundgren and Malmström [71].

### 3.1 General theory of photoemission

In this section, the main features of general photoemission theory will be elucidated. The calculation of the photocurrent starts from first order time-dependent perturbation theory. Assuming a small perturbation  $\Delta$ , the transition probability per unit time  $w$  between two  $N$ -electron states  $|\Psi_F\rangle$  and  $|\Psi_I\rangle$  of the same Hamiltonian  $H$ , is given by Fermi's golden rule:

$$w = \frac{2\pi}{\hbar} |\langle \Psi_F | \Delta | \Psi_I \rangle|^2 \delta(E_F - E_I - \hbar\omega), \quad (7)$$

where  $E_F$  and  $E_I$  denote the energies of the  $N$ -electron states and  $\hbar\omega$  the excitation energy. This equation can be also derived within the Keldysh Green's function approach and can be

represented in the lowest order as a triangular like skeleton diagrams (See e.g. Fujikawa and Arai [72, 73]). In second quantization the interaction operator  $\Delta$  is defined as follows

$$\Delta = \sum_{k,m} \Delta_{k,m} \mathbf{a}_k^\dagger \mathbf{a}_m, \quad (8)$$

where  $\Delta_{k,m}$  denotes a one-particle matrix element between two single-particle states  $\phi_k$  and  $\phi_m$ . The initial and final states are then defined as  $|\Psi_I\rangle = |\Psi_N^0\rangle$  and  $|\Psi_F\rangle = \mathbf{a}_f^\dagger |\Psi_{N-1}^s\rangle$  where  $|\Psi_{N-1}^s\rangle$  denotes an excited  $N - 1$  particle state and  $|\Psi_N^0\rangle$  defines the ground state of the many-particle system. For the explicit formulation of the initial state the so called sudden approximation is used. This means the photoelectron is described by a single-particle state and the interaction with the excited  $N - 1$  state  $|\Psi_{N-1}^s\rangle$  has been completely neglected. In other words  $\mathbf{a}_f |\Psi_N^0\rangle = 0$ . Using these approaches for the initial and final states the transition probability is given by

$$w_s = \frac{2\pi}{\hbar} |\langle \Psi_{N-1}^s | \sum_{k,m} \Delta_{k,m} \mathbf{a}_f \mathbf{a}_k \mathbf{a}_m | \Psi_N^0 \rangle|^2 \delta(E_N - E_{N-1} - \hbar\omega), \quad (9)$$

where the delta-function describes the energy conservation in the photo-excitation process generated by a certain photon energy  $\hbar\omega$ . Performing some standard manipulations on Eq. (9) it follows for  $w = \sum_s w_s$

$$w = \frac{2\pi}{\hbar} \sum_{m,m'} \Delta_{f,m}^\dagger A_{m,m'}(E_n) \Delta_{f,m'}, \quad (10)$$

where

$$A_{m,m'}(E_n) = \frac{2}{\hbar} \sum_s \langle \Psi_N^0 | \mathbf{a}_m^\dagger | \Psi_{N-1}^s \rangle \delta(E_N - E_{N-1} - \hbar\omega) \langle \Psi_{N-1}^s | \mathbf{a}_{m'} | \Psi_N^0 \rangle, \quad (11)$$

represents the one-electron spectral function of the initial state. Using further the relation

$$A_{m,m'}(E_n) = -\frac{1}{\pi} \text{Im} G_{m,m'}^R(E_n) \quad (12)$$

between the spectral function and the one-electron retarded Green's function, the intensity of the photocurrent follows

$$I(\hbar\omega) = -\frac{1}{\pi} \text{Im} \sum_{m,m'} \langle \phi_f | \Delta^\dagger | \phi_m \rangle G_{m,m'}^R(E_n) \langle \phi_m | \Delta | \phi_f \rangle. \quad (13)$$

With the help of the operator representation for  $G^R$

$$G^R(E_n) = \sum_{m,m'} |\phi_m\rangle G_{m,m'}^R(E_n) \langle \phi_{m'}| \quad (14)$$

we arrive at the final expression

$$I(\hbar\omega) = -\frac{1}{\pi} \text{Im} \langle \phi_f | \Delta^\dagger G^R(E_n) \Delta | \phi_f \rangle \quad (15)$$

for the photocurrent  $I(\hbar\omega)$ . Replacing the retarded one-electron Green's function by the one-particle Green function and reformulating Eq. (15) in the space representation one arrives at the one-step model description of the photocurrent as derived among others by Pendry [11] (see Eq. (16) and [74]).

### 3.2 Fully relativistic one-step model of photoemission for alloys

In this section we will show some basic ideas concerning the implementation of Eq. (15) as derived in Sec. 3.1. As a detailed description of the one-step model of photoemission can be found in various reviews (e.g. [17]), here we would like to show only the main steps with an emphasis on the calculations of the photoemission for correlated alloys.

An implementation of the one-step model of PES can be based on Pendry's expression for the photocurrent [11], which is nothing but the space representation of Eq. (15)

$$I^{\text{PES}} \propto \text{Im} \langle \varepsilon_f, \vec{k}_{\parallel} | G_2^+ \Delta G_1^+ \Delta^\dagger G_2^- | \varepsilon_f, \vec{k}_{\parallel} \rangle. \quad (16)$$

$I^{\text{PES}}$  denotes the elastic part of the photocurrent with vertex renormalizations being neglected. This excludes inelastic energy losses and corresponding quantum-mechanical interference terms [11,74,6]. Furthermore, the interaction of the outgoing photoelectron with the rest of the system is not taken into account. This *sudden approximation* is expected to be justified for not too small photon energies. Considering an energy-, angle- and spin-resolved photoemission experiment the state of the photoelectron at the detector is written as  $|\varepsilon_f, \vec{k}_{\parallel}\rangle$ , where  $\vec{k}_{\parallel}$  is the component of the wave vector parallel to the surface, and  $\varepsilon_f$  is the kinetic energy of the photoelectron. The spin character of the photoelectron is implicitly included in  $|\varepsilon_f, \vec{k}_{\parallel}\rangle$  which is understood as a four-component Dirac spinor. The advanced Green's function  $G_2^-$  in Eq. (16) characterizes the scattering properties of the material at the final-state energy  $E_2 \equiv \varepsilon_f$ . Via  $|\Psi_f\rangle = G_2^- |\varepsilon_f, \vec{k}_{\parallel}\rangle$  all multiple-scattering corrections are formally included. For an appropriate description of the photoemission process we must ensure the correct asymptotic behavior of  $\Psi_f(\vec{r})$  beyond the crystal surface, i.e., a single outgoing plane wave characterized by  $\varepsilon_f$  and  $\vec{k}_{\parallel}$ . Furthermore, the damping of the final state due to the imaginary part of the inner potential  $iV_{0i}(E_2)$  must be taken into account. We thus construct the final state within spin-polarized low-energy electron diffraction (SPLEED) theory considering a single plane wave  $|\varepsilon_f, \vec{k}_{\parallel}\rangle$  advancing onto the crystal surface. Using the standard layer-KKR method generalized for the relativistic case [17, 75], we first obtain the SPLEED state  $-T\Psi_f(\vec{r})$ . The final state is then given as the time-reversed SPLEED state ( $T = -i\sigma_y K$  is the relativistic time inversion operator). Many-body effects are included phenomenologically in the SPLEED calculation by using a parametrized weakly energy-dependent and complex inner potential  $V_0(E_2) = V_{0r}(E_2) + iV_{0i}(E_2)$  [13]. This generalized inner potential takes into account inelastic corrections to the elastic photocurrent [74] as well as the actual (real) inner potential, which serves as a reference energy inside the solid with respect to the vacuum level [76]. Due to the finite imaginary part  $iV_{0i}(E_2)$ , the flux of elastically scattered electrons is continuously reduced, and thus the amplitude of the high-energy wave field  $\Psi_f(\vec{r})$  can be neglected beyond a certain distance from the surface (see right panel of Fig. 3).

In the last part of this section we would like to explicitly evaluate Eq. (16) for the CPA photocurrent. A more detailed description of the generalized one-step model for disordered magnetic alloys can be found in Braun *et al.* and Durham *et al.* [36, 26, 20]. The first step in an explicit calculation of the photocurrent consists in the setup of the relativistic spin-polarized

low energy electron diffraction (SPLEED)-formalism within the CPA theory. The coherent scattering matrix  $t_n^{CPA}$  for the  $n$ th atomic site together with the crystal geometry determines the scattering matrix  $M$  for a certain layer of the semi-infinite half-space

$$M_{\mathbf{g}\mathbf{g}'}^{\tau\tau's's'} = \delta_{\mathbf{g}\mathbf{g}'}^{\tau\tau's's'} + \frac{8\pi^2}{kk_{\mathbf{g}z}^+} \sum_{\substack{nn' \\ \Lambda\Lambda'\Lambda''}} i^{-l} C_{\Lambda}^{m_s} Y_l^{\mu-m_s}(\hat{\mathbf{k}}_{\mathbf{g}}^{\tau}) t_{\Lambda\Lambda''}^{CPA} (1-X)_{\Lambda''\Lambda'}^{-1} i^{l'} C_{\Lambda'}^{m'_s} Y_{l'}^{\mu'-m'_s}(\hat{\mathbf{k}}_{\mathbf{g}'}^{\tau'}) e^{-i(\mathbf{k}_{\mathbf{g}}^{\tau}\mathbf{R}_n + \mathbf{k}_{\mathbf{g}'}^{\tau'}\mathbf{R}_{n'})}, \quad (17)$$

where the  $X$ -matrix represents the Kambe lattice sum, which in turn is directly connected with the multiple scattering path operator  $\tau = tX$ . All quantities are indexed by the reciprocal lattice vectors of the 2D layer  $\mathbf{g}$ , relativistic quantum numbers  $\Lambda$  and site index  $n$  and index  $\tau = \pm$  (+ for transmission, and  $-$  for reflection).  $C$  and  $Y$  are standard Clebsch-Gordan coefficients and the spherical harmonics, respectively. By means of the layer-doubling technique the so called bulk-reflection matrix can be calculated, which gives the scattering properties of a semi-infinite stack of layers. Finally, applying SPLEED theory [44, 77] we are able to derive the final state for the semi-infinite crystal. The quantity  $\Delta$  in Eq. (16) is the dipole operator in the electric dipole approximation. It mediates the coupling of the high-energy final state with the low-energy initial states. In a fully relativistic theory the dipole interaction of an electron with the electromagnetic field is given by the dipole operator  $\Delta = -\alpha\mathbf{A}_0$  where  $\mathbf{A}_0$  is the spatially constant vector potential inside the crystal. The three components  $\alpha_k$  of the vector  $\alpha$  are defined through the tensor product  $\alpha_k = \sigma_1 \otimes \sigma_k$ ,  $k = z, y, z$ , where  $\sigma_k$  denote the Pauli spin matrices. Dealing with the matrix element  $\langle \Psi_f | \Delta | \Psi_i \rangle$  between eigenspinors  $|\Psi_f\rangle$  and  $|\Psi_i\rangle$  of the Dirac Hamiltonian with energies  $E_f$  and  $E_i$ , respectively, it is numerically more stable to transform  $\Delta$  in the so called  $\nabla V$  form of matrix elements. This is derived by making use of commutator and anticommutator rules analogously to the nonrelativistic case in Ref. [78, 79].

According to Pendry [11] the calculation of  $G_1^+$ , and in consequence the calculation of the photocurrent, can be divided into four different steps. The first contribution  $I^{\text{at}}$ , the so called *atomic contribution* results from the replacement of  $G_1^+$  in Eq. (16) by  $G_{1,a}^+$ . The second contribution  $I^{\text{ms}}$ , describes the multiple scattering of the initial state. The third contribution  $I^{\text{s}}$  to the photocurrent takes care of the surface. When dealing with the disorder in the alloys, an additional  $I^{\text{inc}}$ , the so called *incoherent* term, appears. Following Durham *et al.* [26,20] the configurational average can be written as

$$\langle I^{\text{AR-PES}} \rangle = \frac{1}{\pi} \text{Im} \sum_{ij} \langle M_i \tau^{ij} M_j^* \rangle = \frac{1}{\pi} \text{Im} \sum_i \langle M_i^a \rangle + \langle I^{\text{s}} \rangle. \quad (18)$$

Herein  $\tau^{ij}$  denotes the scattering path operator between the sites  $i$  and  $j$ .  $M_i^a$  represents an atomic-type matrix element containing the irregular solutions which appear as a part of the retarded Green function  $G_{1,a}^+$ .  $M_i$  indicates a conventional matrix element between regular solutions of the initial and final states. The first term can be decomposed in on-site and off-site contributions

$$\sum_{ij} \langle M_i \tau^{ij} M_j^* \rangle = \sum_{ij, i \neq j} \langle M_i \tau^{ij} M_j^* \rangle + \sum_i \langle M_i \tau^{ii} M_i^* \rangle. \quad (19)$$

The on-site term is called incoherent part of the photocurrent since this term reveals density-of-states (DOS)-like behavior by definition. The off-site contribution which contains all dispersing features represents the so called coherent part of the photocurrent. Together with the surface part that remains unchanged by the averaging procedure  $\langle I^s \rangle = I^s$  the total one-step current can be written as

$$\begin{aligned} \langle I^{\text{AR-PES}} \rangle &= -\frac{1}{\pi} \text{Im} \sum_i \langle M_i^a \rangle + I^s \\ &+ \frac{1}{\pi} \text{Im} \sum_{ij, i \neq j} \langle M_i \tau^{ij} M_j^* \rangle \\ &+ \frac{1}{\pi} \text{Im} \sum_i \langle M_i \tau^{ii} M_i^* \rangle . \end{aligned} \quad (20)$$

Using Pendry's notation it follows

$$\langle I^{\text{AR-PES}}(\varepsilon_f, \mathbf{k}) \rangle = \langle I^{\text{at}}(\varepsilon_f, \mathbf{k}) \rangle + \langle I^{\text{ms}}(\varepsilon_f, \mathbf{k}) \rangle + \langle I^{\text{inc}}(\varepsilon_f, \mathbf{k}) \rangle + I^s(\varepsilon_f, \mathbf{k}), \quad (21)$$

where  $I^{\text{ms}}$  can be identified with the coherent contribution that describes all band-like features of the initial state and  $I^{\text{inc}}$  with the incoherent contribution that describes the corresponding DOS-like features. Because of this clear-cut separation in contributions that describe dispersing or non-dispersing features one may easily define the angle-integrated photocurrent by use of the CPA-formalism. The ordered case is then defined by a binary alloy with two identical species at each atomic site. Therefore, it follows

$$\langle I^{\text{AI-PES}}(\varepsilon_f, \mathbf{k}) \rangle = \langle I^{\text{at}}(\varepsilon_f, \mathbf{k}) \rangle + \langle I^{\text{inc}}(\varepsilon_f, \mathbf{k}) \rangle + I^s(\varepsilon_f, \mathbf{k}). \quad (22)$$

For the atomic contribution the averaging procedure is trivial, since  $\langle I^{\text{at}}(\varepsilon_f, \mathbf{k}) \rangle$  is a single-site quantity. In detail, the atomic contribution is build up by a product between the matrix  $\mathcal{Z}_{jn\alpha_n}^{\text{at}}$  and the coherent multiple scattering coefficients  $A_{jn\Lambda}^c$  of the final state. Herein  $n$  denotes the  $n$ th cell of the  $j$ th layer and  $\Lambda$  denotes the combined relativistic quantum numbers  $(\kappa, \mu)$ . It follows

$$\langle I^{\text{at}}(\varepsilon_f, \mathbf{k}) \rangle \propto \text{Im} \sum_{\substack{jn\alpha_n \\ \Lambda\Lambda'}} x_{jn\alpha_n} A_{jn\Lambda}^c \mathcal{Z}_{jn\alpha_n}^{\text{at}} A_{jn\Lambda'}^{c*}, \quad (23)$$

where  $\alpha_n$  denotes the different atomic species located at a given atomic site  $n$  of the  $j$ th layer. The corresponding concentration is given by  $x_{jn\alpha_n}$ .

For an explicit calculation  $\mathcal{Z}^{\text{at}}$  must be separated into angular matrix elements and radial double matrix elements. A detailed description of the matrix  $\mathcal{Z}^{\text{at}}$  and of the multiple scattering coefficients  $A_{jn\Lambda}^c$  for the different atomic species is given in Refs. [17, 75].

The intra(inter)-layer contributions  $\langle I^{\text{ms}}(\varepsilon_f, \mathbf{k}) \rangle$  to the photocurrent describe the multiple scattering corrections of the initial state  $G_1^+$  between and within the layers of the single crystal. They can be written in a similar form

$$\langle I^{\text{ms}}(\varepsilon_f, \mathbf{k}) \rangle \propto \text{Im} \sum_{\substack{jn \\ \Lambda\Lambda'}} A_{jn\Lambda}^c \mathcal{Z}_{jn}^{c(2)} C_{jn\Lambda'}^{B,G}. \quad (24)$$

In analogy to the atomic contribution, the coherent matrix  $\mathcal{Z}^{c(2)}$  can be separated into angular- and radial parts. The difference to the atomic contribution is that the radial part of the matrix  $\mathcal{Z}^{c(2)}$  consists of radial single matrix elements instead of radial double integrals. In the alloy case this matrix results in the following expression

$$\mathcal{Z}_{\Lambda\Lambda'}^{c(2)} = \sum_{\substack{\alpha_n \\ \Lambda_1\Lambda_2\Lambda_3}} x_{jn\alpha_n} D_{\Lambda_1\Lambda_2} R_{\Lambda_1\Lambda\Lambda_2\Lambda_3}^{(2)} \mathcal{D}_{\Lambda_3\Lambda'}^{jn\alpha_n}. \quad (25)$$

The radial and angular parts of the matrix element are denoted by  $R^{(2)}$  and  $D$ . The CPA-average procedure explicitly is represented in terms of the CPA-projector  $\mathcal{D}_{jn\alpha_n}$  representing the  $\alpha$ -species at site  $n$  for layer  $j$ .  $C^B$  and  $C^G$  denote the coherent multiple scattering coefficients of the initial state within a layer and between different layers. They have the form

$$C_{jn\Lambda}^B = \sum_{n'\Lambda'\Lambda''} B_{jn'\Lambda'}^{(o)c} (t^{CPA})_{\Lambda'\Lambda''}^{-1} \left( (1-X)_{\Lambda''\Lambda}^{-1} - \delta_{\Lambda''\Lambda'} \right), \quad (26)$$

with the coherent bare amplitudes  $B_{jn'\Lambda'}^{(o)c}$

$$B_{jn'\Lambda'}^{(o)c} = \sum_{\Lambda''} \mathcal{Z}_{\Lambda'\Lambda''}^{c(1)} A_{jn'\Lambda''}^{c*}. \quad (27)$$

and

$$\mathcal{Z}_{\Lambda\Lambda'}^{c(1)} = \sum_{\substack{\alpha_n \\ \Lambda_1\Lambda_2\Lambda_3}} x_{jn\alpha_n} \mathcal{D}_{\Lambda\Lambda_3}^{\dagger} R_{\Lambda_1\Lambda_3\Lambda_2\Lambda'}^{(1)} D_{\Lambda_1\Lambda_2}^{\dagger}. \quad (28)$$

Finally, the coherent scattering coefficients  $C^G$  for the inter-layer contribution take the form

$$C_{jn\Lambda}^G = \sum_{n'\Lambda'} G_{jn'\Lambda'}^{(o)c} (1-X)_{\Lambda'\Lambda}^{-1} \quad (29)$$

and the coherent bare amplitudes  $G_{jn'\Lambda'}^{(o)c}$  are given by

$$G_{jn'\Lambda'}^{(o)c} = \sum_{\mathbf{g}m_s} 4\pi i^{l'} (-)^{\mu'-s} C_{\Lambda'}^{m_s} (d_{j\mathbf{g}m_s}^+ Y_{l'}^{m_s-\mu'}(\widehat{k_{1\mathbf{g}}^+}) e^{i\mathbf{k}_{1\mathbf{g}}^+ \cdot \mathbf{r}_{n'}} + d_{j\mathbf{g}m_s}^- Y_{l'}^{m_s-\mu'}(\widehat{k_{1\mathbf{g}}^-}) e^{i\mathbf{k}_{1\mathbf{g}}^- \cdot \mathbf{r}_{n'}}). \quad (30)$$

The coefficients  $d_{j\mathbf{g}m_s}^{\pm}$  in Eq. (30) represent the plane-wave expansion of the initial state between the different layers of the semi-infinite stack of layers. For a detailed description of the matrices  $\mathcal{Z}^{\text{at}}$ ,  $\mathcal{Z}^{(1)}$  and  $\mathcal{Z}^{(2)}$  and of the multiple scattering coefficients  $d_{j\mathbf{g}m_s}^{\pm}$  the reader again is referred to Refs. [17, 75].

The last contribution to the alloy photocurrent is the so called incoherent part  $\langle I^{\text{inc}}(\varepsilon_f, \mathbf{k}) \rangle$ , which appears because the spectral function of an disordered alloy [45] is defined as a non single-site quantity. In fact this contribution is closely connected with the presence of the irregular wave functions well-known from the spherical representation of the Green function  $G_1^+$ .

The incoherent term is defined as

$$\begin{aligned}
\langle I^{\text{inc}}(\varepsilon_f, \mathbf{k}) \rangle &\propto \text{Im} \sum_{\substack{jn\alpha_n \\ \Lambda\Lambda'\Lambda''}} x_{jn\alpha_n} A_{jn\Lambda}^c \mathcal{Z}_{jn\alpha_n}^{(1)}(\Lambda\Lambda') (\tau_{jn\alpha_n}^{00} - t_{jn\alpha_n})_{\Lambda'\Lambda''} \mathcal{Z}_{jn\alpha_n}^{(2)}(\Lambda''\Lambda''') A_{jn\Lambda'''}^{c*} \\
&+ \text{Im} \sum_{\substack{jn \\ \Lambda\Lambda'}} A_{jn\Lambda}^c \mathcal{Z}_{jn}^{c(1)}(\Lambda\Lambda') \tau_{c\ jn}^{00} \mathcal{Z}_{jn}^{c(2)}(\Lambda''\Lambda''') A_{jn\Lambda'''}^{c*}, \quad (31)
\end{aligned}$$

where  $\tau_{jn\alpha_n}^{00}$  denotes the one-site restricted average CPA-matrix for species  $\alpha_n$  at atomic site  $n$  for layer  $j$ .  $\tau_{c\ jn}^{00}$  represents the corresponding matrix for the coherent medium. This completes the CPA-averaged photocurrent within the fully-relativistic one-step model.

## 4 LSDA+DMFT for calculations of spectroscopic properties

In the following section we would like to show a couple of recent applications of the formalism presented in Secs. 2 and 3. The propose of the detailed discussion at each example is to show which additional information one can gain from the one-step model calculations in contrast to the standard interpretation of ARPES-spectra-based comparisons between ground state spectral functions or densities of states with experimental data.

### 4.1 Angle-integrated valence band photoemission: Fano effect

Spin-orbit coupling gives rise to many interesting phenomena in the electron spectroscopy of magnetic solids. A rather straightforward access to the understanding of these phenomena is provided by the study of the Fano effect. This effect was predicted by Fano at the end of the sixties and denotes the fact that one obtains a spin-polarized photoelectron current even for non-magnetic systems if the excitation is done using circularly polarized light [80]. Reversing the helicity in non-magnetic samples reverses the spin polarization of the photocurrent. This symmetry is in general broken for magnetically ordered systems leading to magnetic circular dichroism. As a consequence, in the case of magnetic materials, the spin polarization is usually due to the interplay between spin-orbit coupling and exchange splitting. Recently, we demonstrated by investigations on Fe, Co and Ni that the pure Fano effect can also be observed in angle-integrated valence band XPS (VB-XPS) for ferromagnets if circularly polarized light impinges perpendicular to the magnetization direction and if a subsequent spin analysis is done with respect to the direction of the photon beam [81]. This is demonstrated in Fig. 4 where the VB-XPS of Fe, Co and Ni at a photon energy of 600 eV is shown. The photon energy of 600 eV has been used in order to increase the bulk sensitivity of the photoemission process. In the upper panel of Fig. 4 we compare experimental data with corresponding LSDA and LSDA+DMFT VB-XPS data based on the one-step model of photoemission. In all three cases the LSDA+DMFT considerably improves the agreement with experiment. In particular, in the case of Ni LSDA+DMFT leads to a shrinking of the  $d$  band width and to a pronounced increase of the intensity in the regime of the 6 eV satellite. Also, for the total intensity of the Fe and

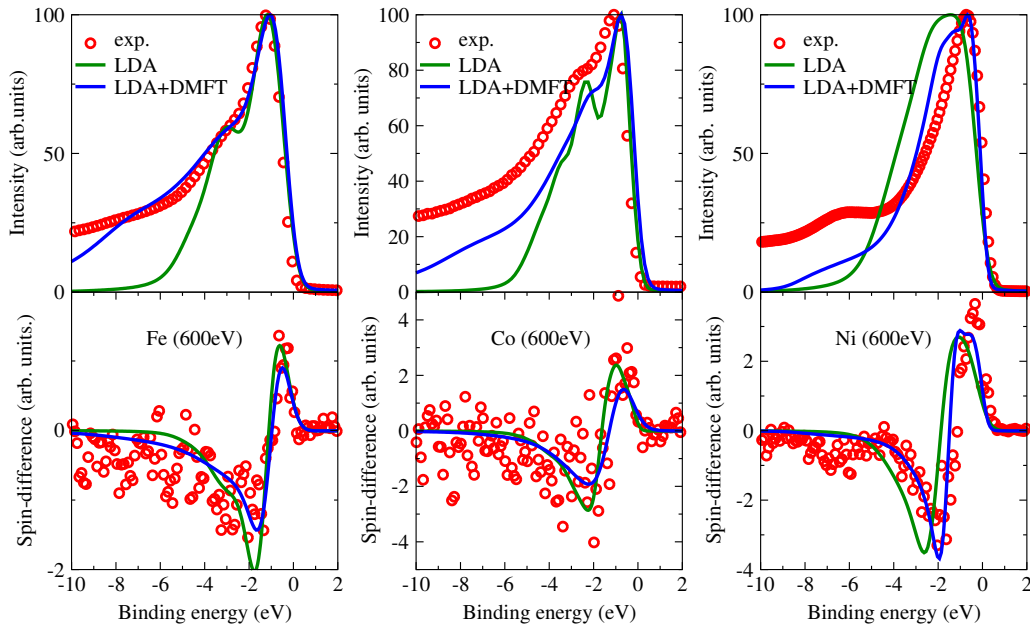


**Fig. 4:** Top panel: The experimental (dots), LSDA (green line) and LSDA+DMFT (blue line) angle integrated valence band XPS spectra of bcc Fe, hcp Co and fcc Ni for a photon energy of 600 eV. Lower panel: Spin difference  $\Delta I^+ = I_{\uparrow}^+ - I_{\downarrow}^+$  of the photocurrent for excitation with left circularly polarized light. Figure reproduced from [81].

Co spectra we observed a pronounced improvement in the energy region from  $-2$  to  $-8$  eV. A decomposition of the theoretical spectrum according to the angular momentum character of the initial state shows that the  $d$ -contribution is by far dominating and that the spectrum essentially maps the corresponding DOS. This, in some sense, supports the common practice of comparing experimental XPS directly with the DOS. In the lower panel of Fig. 4 the corresponding spin difference  $\Delta I^+ = I_{\uparrow}^+ - I_{\downarrow}^+$  (i.e., the difference of the currents of photoelectrons with spin-up and spin-down electrons, for excitation with left circularly polarized radiation) is shown. The occurrence of this spin current is a pure matrix element effect induced by spin-orbit coupling. In fact, one finds that the shape of the  $\Delta I^+$  curves are very similar to those that can be found for non-magnetic noble metals [82, 83]. In fact, the amplitudes scale with the spin-orbit coupling parameter of the Fe, Co and Ni  $d$ -states. To achieve this rather good agreement with the experimental data for the  $\Delta I^+$  intensity distribution the fully self-consistent LSDA+DMFT approach is obviously needed.

## 4.2 ARPES: Correlation effects in transition-metals and their surfaces

In the previous section, we showed angle-integrated XPS spectra which can be directly compared to the DOS ignoring to some extent matrix element effects (upper part of Fig. 4). However, the most detailed mapping of the band structure of correlated materials can be obtained by spin- and angle-resolved valence band photoemission. In the following section we present various examples of angle-resolved photoemission calculations done within the one-step model. These examples clearly demonstrate the need to include matrix-elements in corresponding calculations in order to obtain a quantitative understanding of the experimental data.

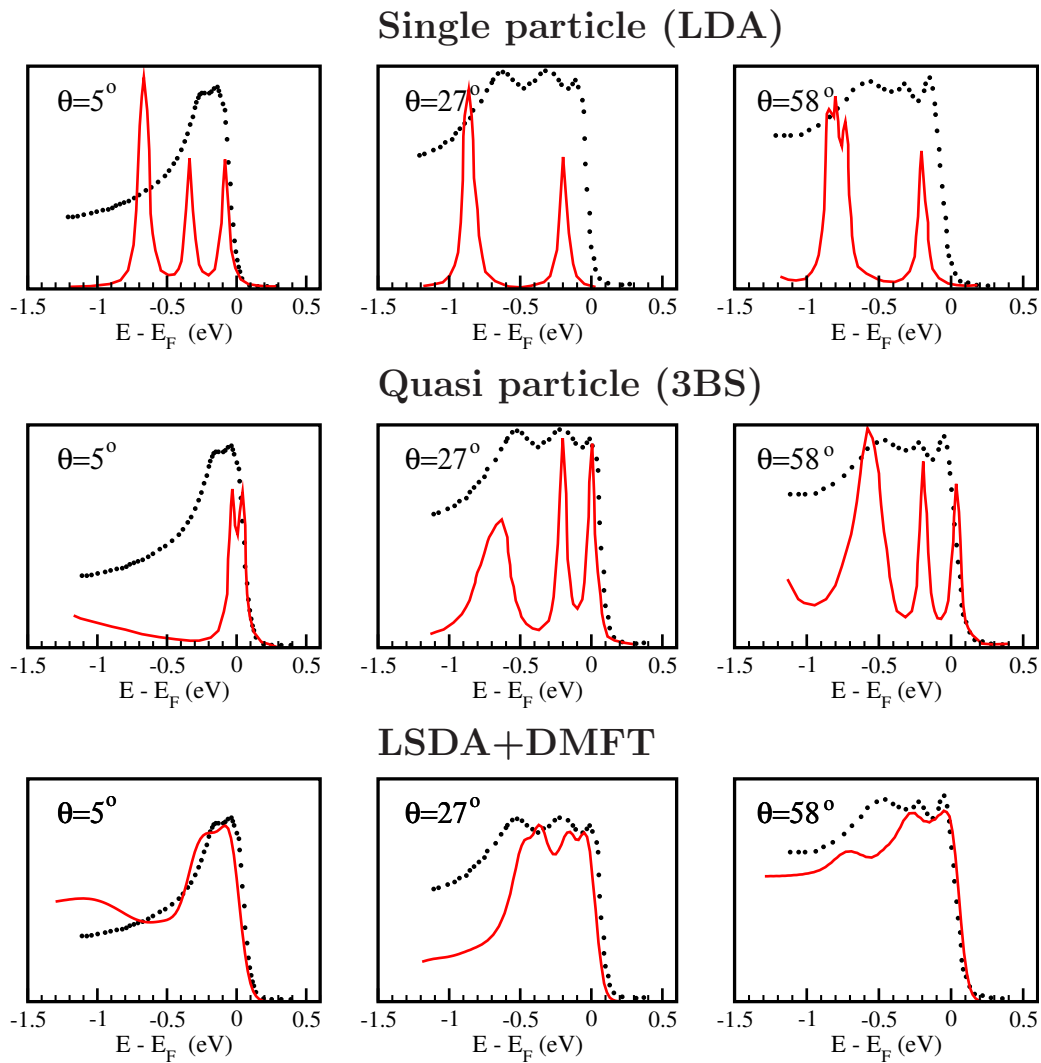


**Fig. 5:** Spin-integrated ARPES spectra from Ni(011) along  $\overline{\Gamma Y}$  for three different angles of emission. Upper row: comparison between LSDA-based calculation and experiment [68]; middle row: comparison between experiment and non self-consistent quasi-particle calculations neglecting matrix element and surface effects [68]; lower row: spin-integrated LSDA+DMFT spectra including photoemission matrix elements (this work). Theory: solid red line, experiment: black dots. Figure reproduced from [38].

The following examples concern the ferromagnetic transition-metal systems Ni and Fe as prototype materials to study electronic correlations and magnetism beyond the LSDA scheme. In particular, the electronic structure of fcc Ni has been subject of numerous experimental [84–90] and theoretical studies [91–93] as a prototype of an itinerant electron ferromagnet, since shortcomings of simple one-electron theory are obvious. LSDA calculations for fcc Ni cannot reproduce various features of the electronic structure of Ni which had been observed experimentally. Besides the fact that valence band photoemission spectra of Ni [94–96] show a reduced  $3d$  band width compared to LSDA calculations [97] the spectra show a dispersionless feature at a

binding energy (BE) of about 6 eV, the so-called 6 eV satellite [84, 85, 98–101], which is not reproducible within the LSDA approach. On the other hand, an improved description of correlation effects for the  $3d$  electrons using many-body techniques [91, 92, 102] or in a more modern view applying the LSDA+DMFT scheme [43, 38] results more or less in the experimental width of the  $3d$ -band complex and furthermore is able to reproduce the 6 eV satellite structure in the valence band region.

In Fig. 5 we present a comparison between experimental photoemission data [68] and calculated spectra using different theoretical approaches [38]. In the upper row spin-integrated ARPES spectra from Ni(011) along  $\overline{TY}$  for different angles of emission are shown. The dotted lines represent the experimental data, whereas the solid lines denote a single-particle representation of the measured spectral function. Obviously, the LSDA-based calculation completely fails to describe the experimental data. The energetic positions of the theoretical peaks deviate strongly from the measured ones. Furthermore, the complicated intensity distributions that appear for higher emission angles are not accounted for by the LSDA-based calculations. In contrast, the non self consistent quasi-particle 3BS calculation provides a significant improvement when compared to the measured spectra. For the complete range of emission angles the energetic peak positions coincide with the experiment within about 0.1 eV. Only the overall shape of the measured spectral intensities deviate from the calculations because of the neglect of multiple scattering and surface-related as well as matrix-element effects. In the experiment the various peaks seem to be more broadened and the spectral weight especially for nearly normal emission is shifted by about 0.1 eV to higher binding energies. In addition it seems that for very high emission angles like  $60^\circ$  an even more complicated peak structure is hidden due to limited experimental resolution. The intensity distributions resulting from the corresponding photoemission calculation are shown in the lower row of Fig. 5. A first inspection reveals a very satisfying quantitative agreement between experiment and theory for all emission angles. Let us concentrate first on the excitation spectrum calculated for the emission angle  $\Theta = 5^\circ$ . The spin-integrated spectrum exhibits a pronounced double-peak structure with binding energies of 0.1 eV and 0.3 eV. The second peak is slightly reduced in intensity which is also in accordance with the experimental findings. Furthermore, the width of the spectral distribution is quantitatively reproduced. The calculated binding energies are related to the real part of the self-energy that corrects the peak positions due to a dynamical renormalization of the quasi-particles which is missing in a typical LSDA-based calculation. The relative intensities of the different peaks, on the other hand, must be attributed to the matrix-element effects which enter our calculations coherently via the one-step model of photoemission. The observed double-peak structure originates from excitation of the spin-split  $d$ -bands in combination with a significant amount of surface-state emission [103]. The two spectra calculated for high emission angles show the spectral distributions more broadened than observed in experiment. An explanation can be given in terms of matrix-element effects, due to the dominating dipole selection rules. The spin-resolved spectra reveal a variety of  $d$ -band excitations in both spin channels, which in consequence lead to the complicated shape of the spectral distributions hardly to be identified in the spin-integrated mode.

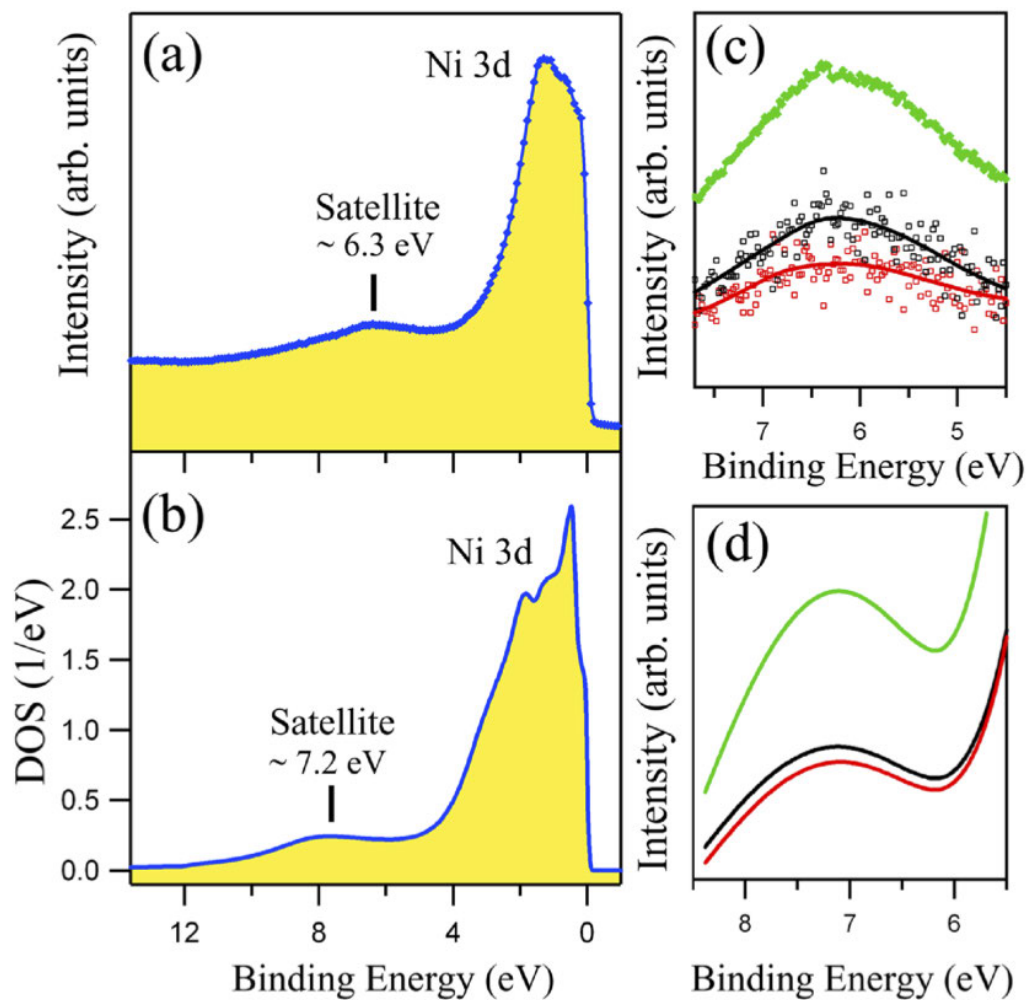


**Fig. 6:** (a) Experimental XPS-spectrum taken at  $h\nu=150$  eV. The “Ni 6 eV satellite” structure appears at about 6.3 eV binding energy. (c) Spin- and angle-resolved photoemission spectra taken in normal emission at  $h\nu=66$  eV with  $s$ -polarized light. Open black squares: majority spin states, open red squares: minority spin states, solid black and red lines serve as guides for the eyes. Spin-integrated intensity: green thick dotted line. (b) LSDA+DMFT calculation of the spin-integrated DOS. The satellite feature appears at about 7.2 eV binding energy. (d) LSDA+DMFT spin-resolved photoemission calculation in normal emission at  $h\nu=66$  eV for a  $U$  value of 3.0 eV: solid black and red lines indicate majority and minority spin states, green line shows the spin-integrated intensity. Figure reproduced from [42].

The second example within this section concerns a spectroscopic study of the 6 eV satellite of Ni. As was shown by earlier calculations [102] and confirmed by photoemission experiments [87], the 6 eV satellite is spin-polarized. In a recent experimental study the XPS intensity at  $h\nu=150$  eV as well as the spin- and angle-resolved photoemission spectra at  $h\nu=66$  eV have been measured. Results for the second experiment are shown in Fig. 6(a) and Fig. 6(c).

The satellite feature is clearly visible at a BE of about 6.3 eV, fully in agreement with all former investigations. Furthermore, Fig. 6(c) shows the non-zero spin-polarization of the satellite in the spin-resolved experiment, again in full agreement with earlier studies [87]. After back-

ground subtraction, the spin polarization amounts to about 15%. In Fig. 6(b) we compare the experimental results with a DOS-calculation which is based on the LSDA+DMFT approach. The parametrization for  $U=2.8$  eV and  $J=0.9$  eV is identical with values that we used for the spin- and angle-resolved photoemission calculations. The satellite appears at a binding energy (BE) of  $\sim 7.2$  eV. This is about 1 eV higher in BE than the experimental result. The explanation for this is found in terms of the many-body solver. The so called FLEX-solver [57] is based on perturbation theory while a more accurate quantum Monte Carlo solver is able to consider the complete diagrammatic expansion of the self-energy in a statistical way. As a consequence the energy dependence of the self-energy is less pronounced and this causes the observed shift of about 1 eV in the BE. Nevertheless, the satellite is observable in the calculated DOS and therefore one would expect its appearance in the theoretical photoemission intensity as well. The corresponding spin- and angle-resolved photoemission calculation is shown in Fig. 6(d). A weak intensity distribution in the vicinity of the  $sp$  band transition is present at a BE of  $\sim 7.2$  eV. The green curve shows the spin-integrated intensity, whereas the black and red lines indicate the majority and minority spin related intensities. The calculated spin-polarization amounts to about 10% slightly smaller than the experimental one. Besides these small deviations between experiment and theory the agreement is very satisfying. Thus we show the first angle-resolved photoemission calculation for Ni metal in which this spectral feature appears.

In conclusion, we have presented a spectroscopical analysis for ferromagnetic Ni and Co, which coherently combine an improved description of electronic correlations with multiple-scattering, surface emission, dipole selection rules and other matrix-element related effects that lead to a modification of the relative photoemission intensities. As has been demonstrated, this approach allows on the one hand side a detailed and reliable interpretation of angle-resolved photoemission spectra of  $3d$ -ferromagnets. On the other hand, it also allows for a very stringent test of new developments in the field of DMFT and similar many-body techniques.

The third example within this section concerns a spectroscopic study of ferromagnetic Fe [40]. In the left panel of Fig. 7 we compare the experimental peak positions from bulk-like transitions with spin-resolved LSDA+DMFT spectral functions. In addition to these investigations correlation effects were also accounted for within the 3BS approach [104]. Within the 3BS approach the self-energy is calculated using a configuration interaction-like expansion. In particular three-particle configurations like one hole plus one electron-hole pair are explicitly taken into account within 3BS-based calculations. The corresponding output can be directly related to the photoemission process and allows for a detailed analysis of various contributions to the self-energy (e.g., electron-hole lifetime). A more detailed quantitative comparison is shown in right panel of Fig. 7. Here we display a comparison between spin-integrated ARPES data and theoretical LSDA+DMFT based one-step photoemission calculations of Fe(110) along the  $\Gamma N$  direction of the bulk Brillouin zone (BZ) with  $p$ -polarized radiation. In our LSDA+DMFT investigation underlying the ARPES calculations we use for the averaged on-site Coulomb interaction  $U$  a value  $U=1.5$  eV which lies between  $U \approx 1$  eV deduced from experiment [105] and the value  $U \approx 2$  eV obtained within other theoretical studies [106,59]. From an analysis of the spectra, the  $k$  values associated with the observed transitions were determined using photon

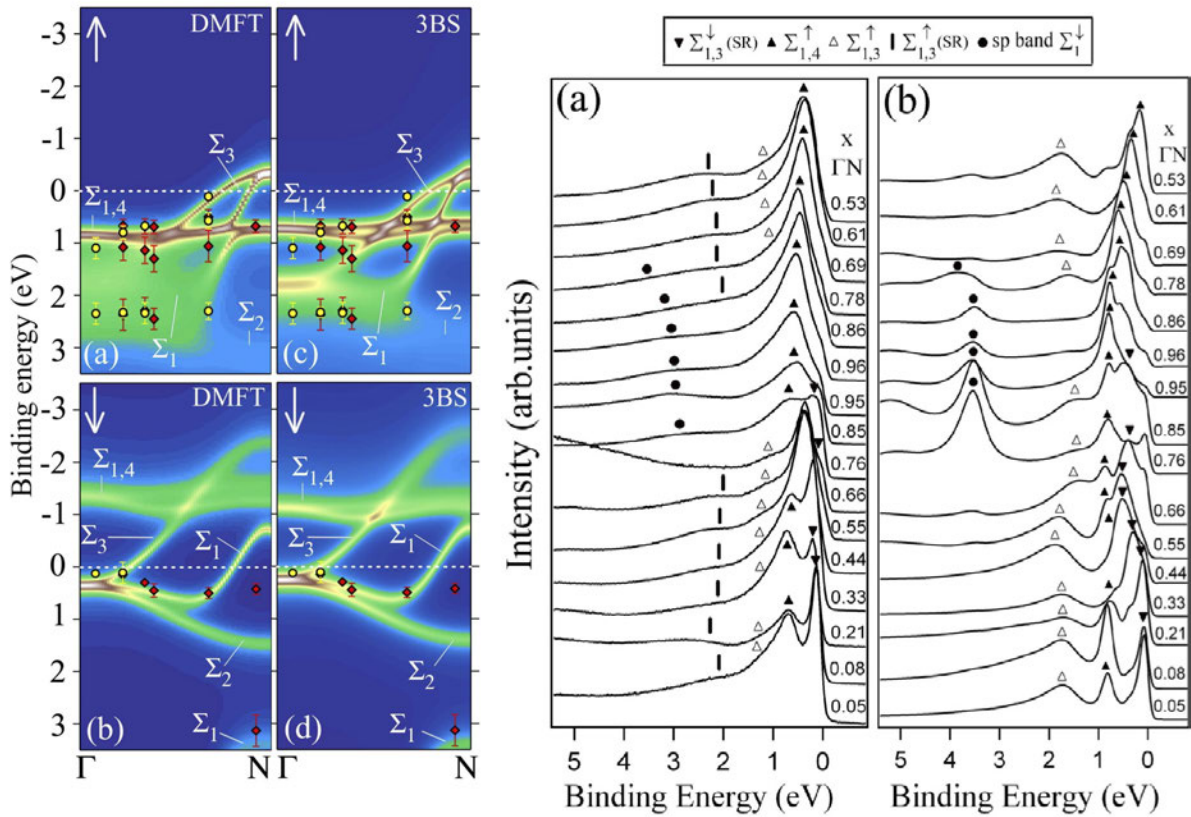


**Fig. 7:** Left panel: Spin resolved Bloch spectral functions calculated within LSDA+DMFT and 3BS formalism. Corresponding experimental data points have been deduced from the normal emission spectra along the  $\Gamma$ N direction. Right panel: (a) Experimental spin-integrated photoemission spectra of the Fe(110) surface measured with p-polarization in normal emission along the  $\Gamma$ N direction of the bulk Brillouin zone. The curves are labeled by the wave vectors in units of  $\Gamma$ N =  $1.55 \text{ \AA}^{-1}$ . (b) Corresponding one-step model calculations based on the LSDA+DMFT method which include correlations, matrix elements and surface effects. Figure reproduced from [40].

energies ranging from 25 to 100 eV. Near the  $\Gamma$  point ( $k \sim 0.06 \Gamma$ N), the intense peak close to the Fermi level corresponds to a  $\Sigma_{1,3}^\downarrow$  minority surface resonance, as indicated in the top of Fig. 7. Experimentally, its  $\Sigma_3^\downarrow$  bulk component crosses the Fermi level at  $k \sim 0.33 \Gamma$ N, leading to a reversal of the measured spin-polarization and to a strong reduction of the intensity at  $k = 0.68 \Gamma$ N in the minority channel. The peak at the binding energy  $BE \sim 0.7 \text{ eV}$ , visible mainly for p-polarization in a large range of wave vectors between  $\Gamma$  and N, can be assigned to almost degenerate  $\Sigma_{1,4}^\uparrow$  bulk-like majority states. A  $\Sigma_3^\uparrow$  feature at  $BE \sim 1.1 \text{ eV}$  dominates the spectrum close to the  $\Gamma$ -point. Depending on the polarization the degenerate  $\Sigma_1^\uparrow$  states form a shoulder around the same BE. The broad feature around 2.2 eV, visible at various  $k$ -points, but not at the N-point, is related to a majority  $\Sigma_{1,3}^\uparrow$  surface state. Around the N-point ( $0.76 \leq k \leq 1.0$ ) and at  $BE \geq 3 \text{ eV}$  we observe a  $\Sigma_1^\downarrow$  band having strong  $sp$  character. The pronounced difference between its theoretical and experimental intensity distributions can be attributed to the fact that

in the present calculations only the local Coulomb repulsion between  $d$  electrons is considered, without additional lifetime effects for the  $sp$  bands. Finally, we notice that the background intensity of the spectrum at  $k=0.66 \Gamma N$ , corresponding to a photon energy of 55 eV, is strongly increased due to the appearance of the Fe  $3p$  resonance. The direct comparison of the calculated and experimental spectra turned out to be a very stringent check for the Coulomb parameter  $U$  used in the calculations. This also applies to the DMFT self-energy, which was compared to its counterpart deduced from the experimental band dispersion and line width.

In summary, spectral function calculations for ferromagnetic Ni and Fe could be performed that coherently combine an improved description of electronic correlations, multiple-scattering, surface emission, dipole selection rules and other matrix-element related effects that lead to a modification of the relative photoemission intensities. A similar study has been performed recently for hcp Co(0001) [60] and fcc Co(001) [107]. The combined approach allows on the one hand side a detailed and reliable interpretation of high-resolution angle-resolved photoemission spectra of  $3d$ -ferromagnets. On the other hand, it also allows for a stringent test of new developments in the field of DMFT and related many-body techniques.

### 4.3 ARPES of disordered correlated alloys: $\text{Ni}_x\text{Pd}_{1-x}$ (001)

In this section, alloying effects in combination with electronic correlations are considered [36]. Fig. 8 shows a series of spectra of  $\text{Ni}_x\text{Pd}_{1-x}$  as a function of the concentration  $x$  calculated for a photon energy  $h\nu = 40$  eV with linearly polarized light. The experimental data are shown in the left panel and the corresponding LSDA+DMFT-based photoemission calculations are presented in the right one. Our theoretical analysis shows that starting from the pure Ni, the agreement is fully quantitative with deviations less than 0.1 eV binding energy, as expected on the basis of the studies presented above. Going to the  $\text{Ni}_{0.80}\text{Pd}_{0.20}$  alloy the agreement is comparably good for binding energies between the Fermi energy and 2 eV. Inspecting the density of states (DOS) for the  $\text{Ni}_{0.80}\text{Pd}_{0.20}$  alloy this fact becomes explainable, because this energy interval represents the Ni-dominated region. The Pd derived states start to appear at about 2 eV below  $E_F$  next to the small dip at the Fermi level. For higher binding energies the agreement is also very good, although a bit more structure is observable in the theoretical spectra especially around 3.5 eV. An explanation for this behavior can be found in terms of lifetime effects. However, it should be mentioned here that the background in the experimental spectra due to secondary electrons was not considered for the theoretical spectra. From the results for  $\text{Ni}_{0.70}\text{Pd}_{0.30}$  it becomes clearly visible that an increasing deviation between theory and experiment occurs with increasing Pd concentration. This can be seen from the spectra for  $\text{Ni}_{0.50}\text{Pd}_{0.50}$  and  $\text{Ni}_{0.30}\text{Pd}_{0.70}$  alloys shown next in the series. This is caused by the Pd  $d$ -states that seem to be slightly shifted to higher binding energies. This is well known from other paramagnetic metals like Ag and can be explained in terms of static correlations in the Pd-states not explicitly considered here. In addition, the spectra of  $\text{Ni}_{0.30}\text{Pd}_{0.70}$  reveal some deviations near the Fermi level. Also, the spectral intensity of the Ni surface resonance, that appears at about 0.5 eV binding energy is underestimated in the calculation when compared to experiment.

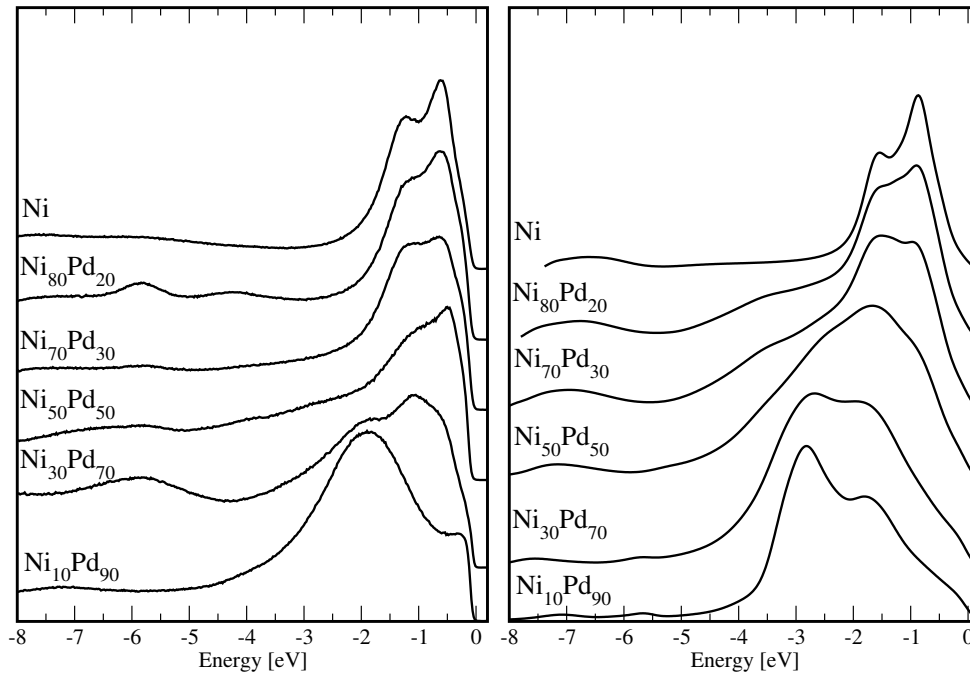


**Fig. 8:** ARPES spectra taken from the  $Ni_xPd_{1-x}(001)$  alloy surfaces as a function of the concentration  $x$  for a fixed photon energy of  $h\nu = 40.0$  eV along  $\Gamma X$  in normal emission. Experimental data shown in the left panel calculated spectra presented in the right panel. Depending on the concentration  $x$  a pronounced shift in spectral weight towards the Fermi level is visible. Figure reproduced from [36].

Our spectroscopic analysis clearly demonstrates that the electronic properties of the  $Ni_xPd_{1-x}$  alloy system depend very sensitively on the interplay of alloying and electronic correlation. A description within the LSDA approach in combination with the CPA results in a quantitative description of the electronic structure of  $Ni_xPd_{1-x}$  [36]. This example may illustrate that the use of the CPA alloy theory self-consistently combined with the LSDA+DMFT approach serves as a powerful tool for electronic structure calculations, whereas the application of the fully relativistic one-step model of photoemission, which takes into account chemical disorder and electronic correlation on equal footing, guarantees a quantitative analysis of corresponding experimental spectroscopic data.

## 5 Angle resolved soft and hard X-ray photomission

It has always been realized, that the results obtained in UV ARPES are restricted in sensitivity to the near-surface region of the systems studied due to the short inelastic mean free paths (IMFPs) of  $\sim 5$ - $10$  Å of the low energy photoelectrons, which are typically in the range from 10-150 eV [108]. To overcome this limitation of surface sensitivity, there is now considerable interest in using x-rays in the soft x-ray sub-keV or even hard x-ray multi-keV regime to access deeper-lying layers in a sample, thus sampling more bulk-like properties [109–119, 27, 29, 30, 32]. One can thus think of soft x-ray or hard x-ray ARPES (HARPES), respectively. These techniques have

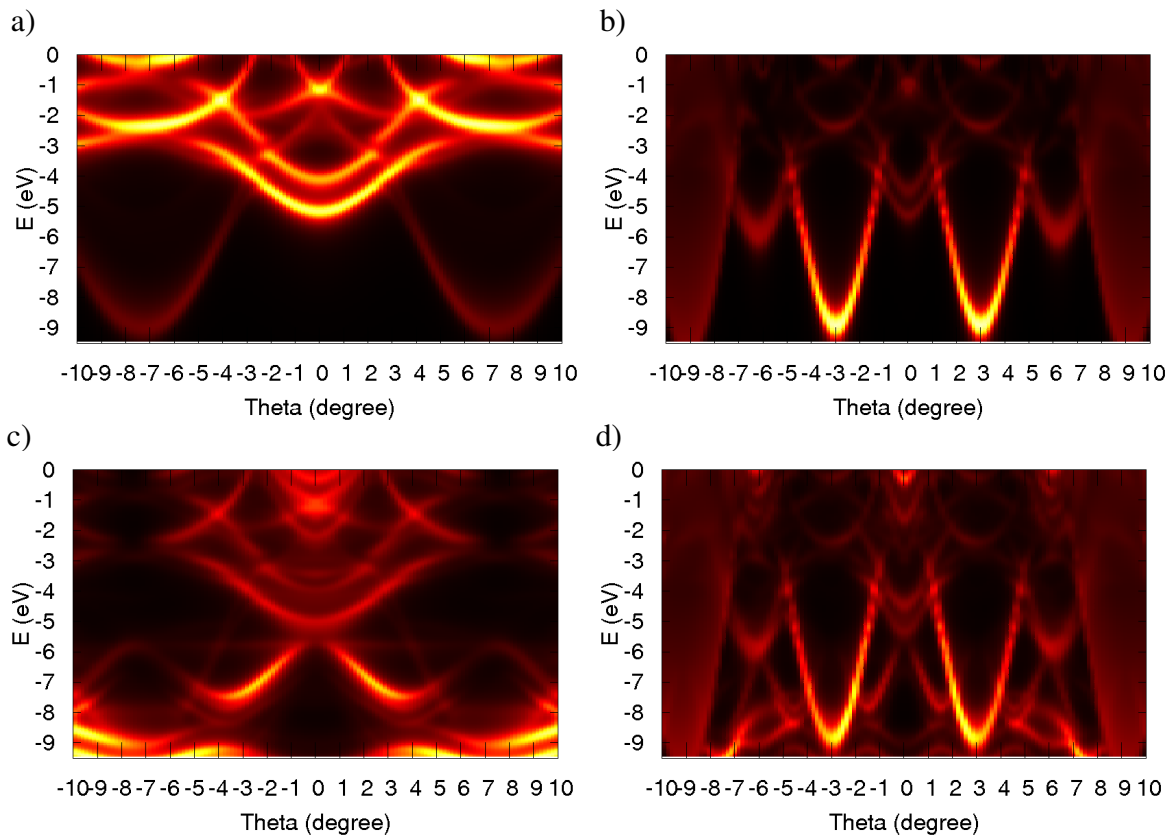


**Fig. 9:** Photoemission spectra calculated for clean Fe(001) (upper panel, a and b). Left side shows the intensity distribution obtained for 1 keV, right side represents the corresponding spectrum at 6 keV. The lower panels show theoretical spectra for the overlayer system 8MgO/Fe(001) at 1 keV (left side, c) and 6 keV (right side, d). Figure reproduced from [120].

to date been applied to a wide variety of materials, including free-electron like and transition-metals [109, 116], strongly correlated oxides and high  $T_C$  materials [111, 112], heavy fermion systems [111], mixed-valent Ce compounds [114], dilute magnetic semiconductors [29,30,121], layered transition-metal dichalcogenides [119]. Additional advantages in such experiments include being able to tune to core-level resonances so as to identify the atomic-orbital makeup of ARPES features [121], to map three-dimensional Fermi surfaces [119], and to take advantage of the longer IMFPs, which translate into less smearing of dispersive features along the emission direction (usually near the surface normal) [118]. Increasing the photon energy means increasing the bulk sensitivity of the corresponding photo emission data. We demonstrate this effect by comparing spectra obtained by photoelectron excitation with 1 keV and 6 keV radiation from the clean Fe(001) surface and from the overlayer system MgO/Fe(100) with 8 ML MgO on Fe. Fig. 9a presents the spectrum for the clean Fe(001) surface and a photon energy of 1 keV. As expected for this photon energy regime, the bulk sensitivity is enhanced and the surface emission is reduced to a negligible extent. Also the relative intensity fraction of the  $sp$ -bands is obviously increased. Going to a much higher photon energy of 6 keV the  $d$ -band intensity is strongly reduced when compared with  $sp$ -band related features. This is shown in Fig. 9b. In a next step we put 8 ML of MgO on the Fe(001) surface and repeat our calculations for both

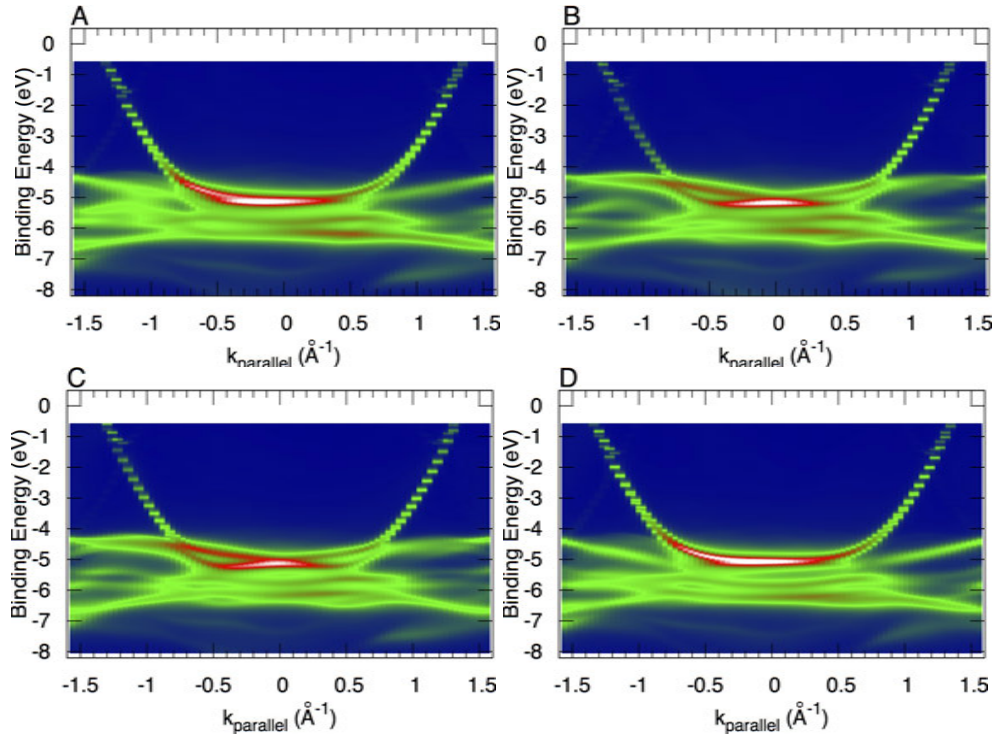
photon energies. This is shown in the lower panel of Fig. 9. At 1 keV mostly the MgO bulk band-structure is visible in Fig. 9c. This is due to the thickness of the MgO film which consists of 8 ML. Increasing the photon energy to 6 keV we expect due to the much larger mean free path length of the photo-electron that Fe-related features will reappear, namely the Fe *sp*-states. This is clearly demonstrated by Fig. 9d which represents the corresponding photo emission spectrum calculated for the 8ML MgO/Fe(001) system at a photon energy of 6 keV. Besides the effect that more than one Brillouin zone is visible for a fixed escape angle regime due to the very high photon energy it is undoubtedly observable that nearly all MgO related features have vanished in the intensity plot. This, for example, should give access to buried interfaces. Going higher in energy, however, comes with some additional challenges for interpretation of the data [109, 115, 118]. Deviations from the dipole approximation in photoelectron excitations mean that the momentum of the photon can result in a non-negligible shift of the position of the initial-state wave vector in the reduced Brillouin zone (BZ) [116]. Also, phonon creation and annihilation during photoemission hinders the unambiguous identification of the initial state in the BZ via wave vector conservation [109, 110, 115, 116, 27, 118, 29].

## 5.1 Photon momentum effects: Ag(001)

Here we want to discuss the effect of the photon momentum  $\mathbf{q}$  on the intensity distribution of the photocurrent. The impact of the photon momentum on the initial state  $\mathbf{k}$ -vector is expressed by the following equation

$$\mathbf{k}_i = \left( \mathbf{k}_{\parallel} - \mathbf{q}_{\parallel} + \mathbf{g}, \sqrt{2(E - iV_{i1}) - |\mathbf{k}_{\parallel} - \mathbf{q}_{\parallel} + \mathbf{g}|^2} \right), \quad (32)$$

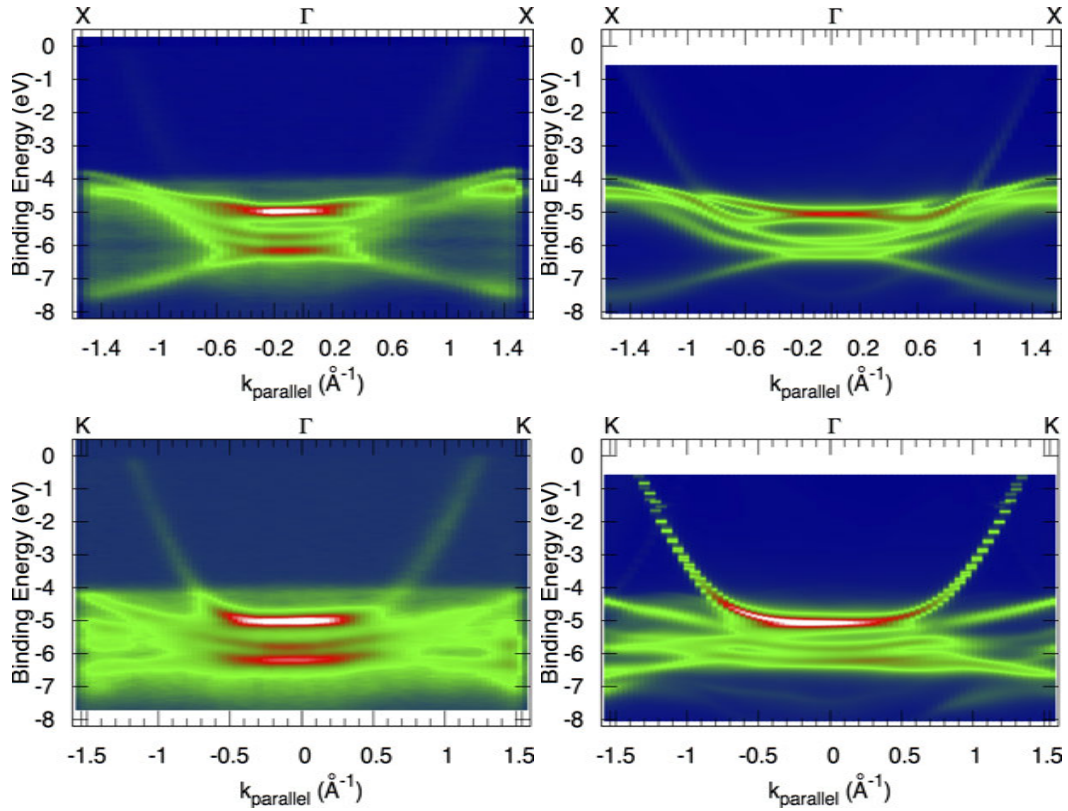
where  $V_{i1}$  denotes the imaginary part of the initial state energy  $E$ . Due to the relatively high photon energies the role played by the photon momentum is no longer negligible, with the importance of its influence depending on the chosen experimental geometry. Considering as an example photo emission from Ag(001), for  $\phi_{ph} = 45^\circ$  the photon momentum has no component along the [110] crystallographic direction. However, the effect of the photon momentum along the  $[\bar{1}10]$  direction is to kick the photo-electron in a direction that is perpendicular to the probed high symmetry direction. This effect can experimentally be corrected for by rotating the crystal surface by a small amount,  $\Theta = 0.7^\circ$ , with respect to the entrance plane of the electron analyzer, thereby minimizing the effect of the photon momentum transfer along the  $[\bar{1}10]$  direction. However, one has to pay the price that the high symmetry plane, in this case the  $\Gamma XUL$  plane, is no longer the plane from which the emission takes place. A careful analysis reveals that an angle  $\Theta = 0.7^\circ$  corresponds, for photon energies in the 500 eV to 600 eV range, to an effective variation of the angle  $\pm 7^\circ$  for the given range of the emission angle  $\theta$  ( $\mathbf{q}_{\parallel}$  effect). Fortunately, the largest deviation appears for nearly normal emission and for higher emission angles it approaches zero. Therefore, the total average deviation from the high symmetry plane is small and the experiment mainly represents emission from the  $\Gamma LUX$  plane with the added advantage of a minimized  $\mathbf{q}_{\parallel}$  effect. Fig. 10 shows the effect of both the correction angle  $\Theta$  and the photon momentum  $\mathbf{q}_{\parallel}$ . In Fig. 10(a) the intensity distribution has been calculated for



**Fig. 10:** Theoretical photo emission intensities for the  $\Gamma$ -K high symmetry direction  $\Sigma$  calculated for  $h\nu=552$  eV,  $\phi = 45^\circ$ . To allow for a one-to-one comparison between experimental and theoretical data, all the theoretical data have been shifted by 1.2 eV. (a) Intensity distribution calculated for  $\mathbf{q}_{\parallel} = 0$  and  $\Theta=0^\circ$ . (b) Intensity distribution calculated for a nonzero  $\mathbf{q}_{\parallel}$  vector and  $\Theta = 0^\circ$ . (c) Intensity distribution calculated for  $\mathbf{q}_{\parallel} = 0$  and  $\Theta = 0.7^\circ$ . (d) Intensity distribution calculated for a nonzero value of  $\mathbf{q}_{\parallel}$  and  $\Theta = 0.7^\circ$ . This corresponds to the experimental geometry setup. Figures taken from [116].

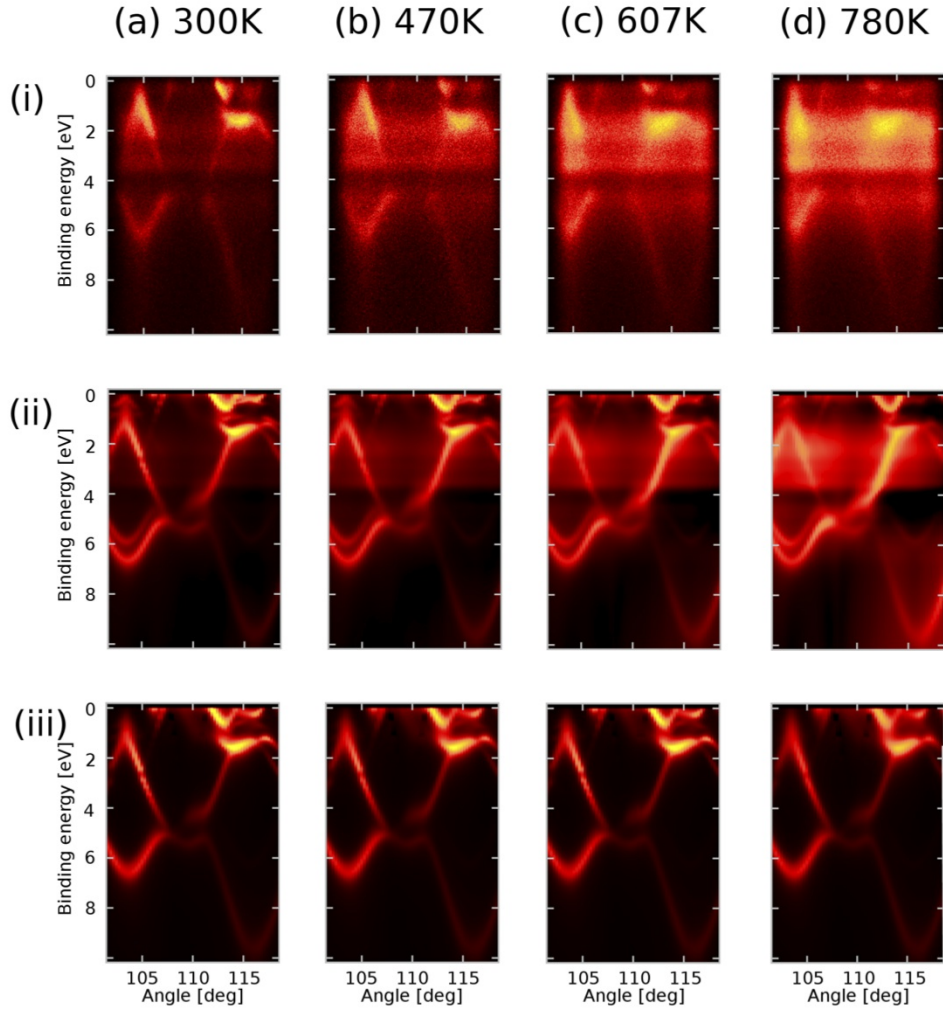
$\Theta = |\mathbf{q}_{\parallel}| = 0$ , whereas in Figs. 10(b) and 10(c) nonzero values for  $\mathbf{q}_{\parallel}$  and  $\Theta$  have been used. It is observable that in both panels 1(b) and 1(c) the band dispersion is more pronounced than in Fig. 10(a), where the bands appear. This effect, together with an additional asymmetric intensity distribution around  $\Gamma$ , is caused by the small deviation from the desired high symmetry plane mentioned above.

Fig. 10(d) represents the experimental situation with  $\Theta = 0.7^\circ$  and a nonzero  $\mathbf{q}_{\parallel}$  value. Observable is the similarity between panels 10(a) and 10(d). Therefore, we can conclude that the experimental procedure works in a satisfactory way. The measurements performed by Venturini *et al.* [116] were taken at  $T = 20$  K for a photon energy of  $h\nu = 552$  eV, that corresponds to the  $\Gamma$  and the X symmetry points along the direction that is perpendicular to the samples surface. The data sets are measured with right circularly polarized light. The results are shown in the left panels of Fig. 11 for  $\phi = 0^\circ$  and  $\phi = 45^\circ$ , respectively. For  $\phi = 0^\circ$ , the parallel component of the initial-state wave vector  $\mathbf{k}_{\parallel}$  varies along the  $\Delta$  direction, whereas for  $\phi = 45^\circ$  the  $\Sigma$  direction is probed. The BZ boundaries along these two directions are found at  $\mathbf{k}_{\parallel} \approx 1.54 \text{ \AA}^{-1}$  and  $\mathbf{k}_{\parallel} \approx 1.63 \text{ \AA}^{-1}$ , respectively, and a photon beam of energy  $h\nu = 552$  eV allows to probe almost the entire BZ along these directions. The experimental results presented in Fig. 11 are in good qualitative agreement with our fully relativistic one-step model photo emission calculations shown in the right panels of the respective figures.



**Fig. 11:**  $\Gamma$ -X high symmetry direction  $\Delta$  probed with  $h\nu = 552, \text{eV}$ ,  $\phi = 0^\circ$  (top) and  $45^\circ$  (bottom), at  $T = 20 \text{ K}$ . The energy refers to the Fermi level  $E_F$ . Left: experimental data. Right: theoretical results. Figures taken from [116].

Along the  $\Delta$  and  $\Sigma$  high symmetry directions, direct transitions originating from all the allowed initial states are visible close to the BZ center, except for the two deeper lying bands along both directions. In particular, for both investigated orientations the  $\Gamma'_{25} \rightarrow \Gamma_8^+ + \Gamma_7^+$  spin-orbit splitting is observed at  $\Gamma$ . The agreement between our calculated binding energies of the high symmetry points along the  $\Gamma$ -X direction [116] and results previously determined in Ref. [122] is very good. Also the agreement with the corresponding experimental values found in literature [123, 122, 124] is good, with a maximum deviation of 0.22 eV for the most tightly bound  $X_6^+$  energy level. The spin-orbit split level with  $X_7^+$  symmetry is barely visible at the BZ boundary along the  $\Delta$  direction (Fig. 11). Its binding energy along this direction is about 4.3 eV (see Ref. [116]). The ARPES data presented so far show evidence of the fact that, for well-defined combinations of  $h\nu$  and temperature, direct transitions in the soft x-ray regime can indeed be observed. If compared to the low energy ARPES, the combination of a larger k-space sampling and a reduced curvature of the investigated path, together with the use of a two-dimensional position sensitive detection system, allow measuring the band structure along specific high symmetry directions with a single measurement. This has been done by Venturini *et al.* [116] for four different high symmetry directions in the BZ of fcc Ag. The corresponding results, which were obtained for  $T = 20 \text{ K}$ , are also in good agreement with our fully relativistic one-step model photo emission calculations.



**Fig. 12:** (i) Plots of measured intensity versus angle of emission for 870 eV excitation from the valence bands of W(110) approximately along the  $\Gamma$ -N direction for four temperatures of (a) 300 K, (b) 470 K, (c) 607 K, and (d) 870 K (from [115]), where 90 deg corresponds to normal emission. (ii) Corresponding intensity distributions calculated from temperature-dependent one-step theory based on the CPA formulation. (iii) Conventional ARPES calculations of the direct contribution  $I^{\text{DT}}(E, \mathbf{k})$  by use of complex scattering phase shifts and the Debye-Waller model). Figure reproduced from [35].

## 5.2 Thermal effects and XPS limit

Going higher in energy, however, comes with some additional challenges for the interpretation of the data [109, 115, 118]. Deviations from the dipole approximation in photoelectron excitation mean that the momentum of the photon can result in a non-negligible shift of the position of the initial-state wave vector in the reduced Brillouin zone (BZ), as first pointed out some time ago. Phonon creation and annihilation during photoemission also hinders the unambiguous specification of the initial state in the BZ via wave vector conservation [118, 115, 116, 27, 29]. Following Shevchik [125], the photoemission intensities at a given energy  $E$  and vector  $\mathbf{k}$  can be approximately divided into zero-phonon direct transitions  $I^{\text{DT}}(E, \mathbf{k})$  and phonon-assisted

non-direct transitions  $I^{\text{NDT}}(E, \mathbf{k})$ . As a rough guide to the degree of direct-transition behavior expected in an ARPES experiment, one can use a temperature-dependent Debye-Waller factor  $W(T)$  which qualitatively represents the fraction of direct transitions [118]. As a first approach that aimed to go beyond this simple scheme for temperature-dependent ARPES, Larsson and Pendry [126] introduced a model called Debye-Waller model later on that incorporates the effect of lattice vibrations on the photoemission matrix elements. More than 15 years later Zampieri *et al.* [127] introduced a cluster approach to model the temperature-dependent excitation of valence band electrons for photon energies of about 1 keV. More recently Fujikawa and Arai [73] discussed phonon effects on ARPES spectra on the basis of nonequilibrium Green's function theory. Recently, we presented a new approach which accurately models phonon effects over the full energy range from normal low-energy ARPES to HARPES. More importantly it converges for high temperatures and/or photon energies to the so called XPS-limit in photoemission, in particular the development of matrix-element weighted density-of-states (MEW-DOS)-like features in the intensity distribution [27, 28]. Our alloy analogy model includes vibrational atomic displacements via the coherent potential approximation (CPA), where vibrations of different lattice sites are assumed to be uncorrelated and averaged in the sense of CPA over various possible displacements which are calculated within Debye theory. Using the CPA-formulation of the one-step model [26, 20, 36] provides a self-consistent temperature-dependent averaging of the photoemission matrix elements. In other words, we describe in a quantitative sense the breakdown of the  $\mathbf{k}$ -conserving rules due to phonon-assisted transitions, the driving mechanism that leads finally to the XPS-limit. In order to demonstrate this effect below we present an example of soft-x-ray ARPES calculations for W(110). In Fig. 12, we compare results of our calculations directly to experimental data for W(110) with soft x-ray excitation at 870 eV [115]. W has a Debye temperature of 400 K and a atomic mass of 183.84 u, close to Au and Pt. In Fig. 12(i), we show experimental results for four different sample temperatures: (a) 300 K, (b) 470 K, (c) 607 K and (d) 780 K [115]. For all four temperatures, dispersive features are clearly seen but with significant smearing and an increase of MEW-DOS-like intensity features as temperature is raised. Also shown in Fig. 13(a), (b) are vertical and horizontal cuts, respectively, through the 2D data of Fig. 12(i). These cuts yield Fig. 13(a): energy distribution curves (EDCs) and Fig. 13(b): momentum distribution curves (MDCs) to illustrate more directly the changes in both types of distributions with temperature. Also, various spectral features are labeled by the numbers 1-6 in these figures. Fig. 12(ii) again presents fully relativistic one-step calculations which are done with our new alloy analogy model, whereas Fig. 12(iii) shows conventional one-step calculations in which phonon excitations are considered in a simplified way through a temperature-dependent single-site scattering matrix [77]. Although at the lowest temperature of 300 K the two different theoretical approaches yield very similar results, as expected for a Debye-Waller factor of 0.70, the temperature dependence of the experimental data is much better described by our temperature-dependent one-step calculations. The simpler calculation based on the single-site scattering matrix predicts neither the smearing of dispersing features nor the growth of MEW-DOS features for higher binding energies, but shows instead only the monotonous decrease of direct transition intensities with increasing temperature [115].

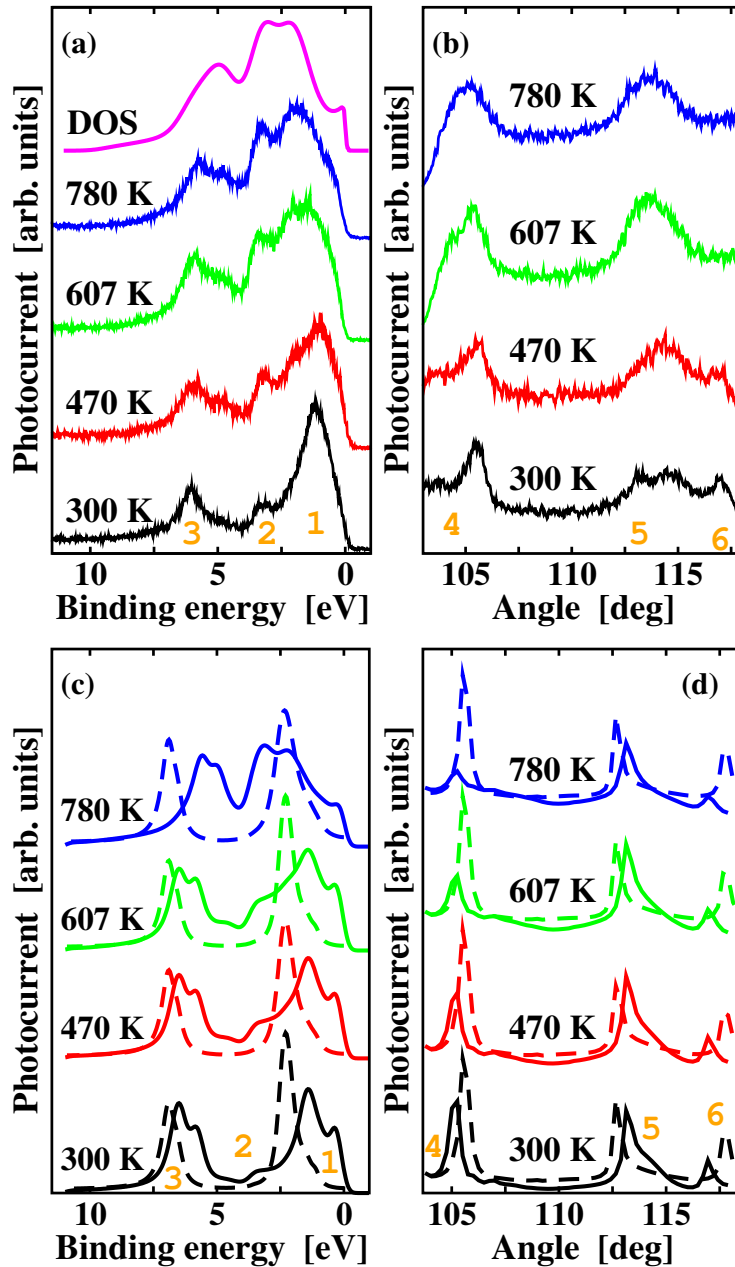


**Fig. 13:** (a) Measured temperature-dependent energy distribution curves (EDCs). A comparison to the W DOS (the topmost curve) is also given. (b) Measured temperature-dependent momentum distribution curves (MDCs). (c), (d) Corresponding theoretical results for (c) EDCs and (d) MDCs. Dashed lines indicate conventional one-step calculations, solid lines indicate calculations within the new alloy analogy model. Figure reproduced from [35].

Phonon induced smearing only appears via temperature-dependent matrix elements which cause a decrease of the direct part of the photocurrent due to a redistribution of spectral weight. Although for 780 K and a photon energy of 870 eV the XPS-limit is not fully established for W, the indirect contribution of the temperature-dependent CPA-like photocurrent dominates the corresponding angle-resolved soft x-ray spectra. This is clearly observable from both the experimental and theoretical data, which are nearly in quantitative agreement.

Figs. 13(a) and (c) compare in more detail the temperature dependence of experimental and theoretical spectra in the form of EDCs for a fixed angle of  $\approx 104$  deg which is 14 deg from the surface normal. Figs. 13(b) and (d) present the same comparison for MDCs at a fixed binding energy of  $\approx 2$  eV. The points labeled 1, 2, 4, 5 and 6 denote *d*-like electronic states, whereas point 3 labels bands that are more free-electron like and a mixture of *s* and *d* states. The experimental and theoretical data in Fig. 12 show pronounced smearing of features in both EDCs and MDCs as the temperature is raised, but some remnant direct-transition behavior is clearly still present, even at 780 K. The dashed lines shown in Fig. 13(c) and (d) indicate conventional one-step calculations using the one-site scattering matrix approach. As expected, only slight changes appear in the form of the EDCs and MDCs as a function of temperature. In contrast, the EDCs and MDCs strongly depend on temperature when using the alloy analogy approach, although in general the MDCs in experiment and those of the conventional and CPA approaches change less than the EDCs. Significant broadening of spectral features and shift of spectral weight, not at all present in the conventional one-site scattering matrix approach, can be observed. The EDC at the highest temperature has not converged to a MEW-DOS-like curve and the corresponding MDC still has structure in it. In the XPS-limit all MDCs would exhibit only x-ray photoelectron diffraction (XPD), with a different type of angular distribution [115, 29, 32, 127, 28]. This is obviously not the case. This is expected, because the Debye-Waller factor of 0.41 at 780 K indicates that a certain number of transitions should still be direct. Our calculations thus correctly predict a diminution of the features expected due to direct transitions, and also a significant broadening of features in the EDCs or MDCs. The additional weak and smooth background observed in the experimental data thus must be ascribed to additional phonon effects, perhaps through multiple phonon excitations.

## 6 Summary

The implementation of the LSDA+DMFT on the basis of the KKR method has been described in some detail. The appealing feature of this approach is that the KKR delivers the one-electron Green's function directly. It therefore allows to combine the treatment of correlations via the DMFT with calculation of a great variety of physical properties for, in principle, any type of system. Within the one-step model of photoemission, this method can be applied to directly calculate ARPES in the wide photon energy range. As was demonstrated by results for photo emission spectra of various transition-metal systems, this allows in particular a direct comparison with experiment.

## Acknowledgement

I would like to thank Jürgen Braun and Hubert Ebert for their stimulating discussions and detailed comments and suggestions to this manuscript. This work was supported by the Deutsche Forschungsgemeinschaft through FOR 1346, by the BMBF (Project 05K13WMA) and CEN-TEM (CZ.1.05/2.1.00/03.0088).

## References

- [1] F. Reinert and S. Hüfner: *Photoemission Spectroscopy with Very High Energy Resolution* Lecture Notes in Physics, Vol. 715 (Springer, Berlin, 2007) p. 13
- [2] A. Damascelli, Z. Hussain, and Z.-X. Shen, *Rev. Mod. Phys.* **75**, 473 (2003)
- [3] I. Adawi, *Phys. Rev.* **134**, A788 (1964)
- [4] G.D. Mahan, *Phys. Rev. B* **2**, 4334 (1970)
- [5] W. Schaich and N. Ashcroft, *Solid State Commun.* **8**, 1959 (1970)
- [6] C. Caroli, D. Lederer-Rozenblatt, B. Roulet, and D. Saint-James, *Phys. Rev. B* **8**, 4552 (1973)
- [7] P.J. Feibelman and D.E. Eastman, *Phys. Rev. B* **10**, 4932 (1974)
- [8] C.N. Berglund and W.E. Spicer, *Phys. Rev.* **136**, A1030 (1964)
- [9] A. Liebsch, *Phys. Rev. Lett.* **32**, 1203 (1974)
- [10] D.J. Spanjaard, D.W. Jepsen, and P.M. Marcus, *Phys. Rev. B* **15**, 1728 (1977)
- [11] J.B. Pendry, *Surf. Sci.* **57**, 679 (1976)
- [12] J.F.L. Hopkinson, J.B. Pendry, and D.J. Titterington, *Comp. Phys. Commun.* **19**, 69 (1980)
- [13] J.B. Pendry: *Low energy electron diffraction* (Academic Press, London, 1974)
- [14] P. Hohenberg and W. Kohn, *Phys. Rev.* **136**, B 864 (1964)
- [15] W. Kohn and L.J. Sham, *Phys. Rev.* **140**, A 1133 (1965)
- [16] L.J. Sham and W. Kohn, *Phys. Rev.* **145**, 561 (1966)
- [17] J. Braun, *Rep. Prog. Phys.* **59**, 1267 (1996)
- [18] B. Ackermann and R. Feder, *J. Phys. C: Solid State Phys.* **18**, 1093 (1985)
- [19] J. Braun, G. Thörner, and G. Borstel, *phys. stat. sol. (b)* **130**, 643 (1985)
- [20] B. Ginatempo, P.J. Durham, and B.I. Gyorffy, *J. Phys.: Condens. Matter* **1**, 6483 (1989)
- [21] S.V. Halilov, E. Tamura, D. Meinert, H. Gollisch, and R. Feder, *J. Phys.: Condens. Matter* **5**, 3859 (1993)
- [22] J. Braun and G. Borstel, *Phys. Rev. B* **48**, 14373 (1993).

- [23] M. Fluchtmann, M. Grass, J. Braun, and G. Borstel, *Phys. Rev. B* **52**, 9564 (1995)
- [24] J. Henk, T. Scheunemann, S.V. Halilov, and R. Feder, *J. Phys.: Condens. Matter* **8**, 47 (1996)
- [25] M. Grass, J. Braun, and G. Borstel, *Prog. Surf. Sci.* **46**, 107 (1994)
- [26] P.J. Durham, *J. Phys. F: Met. Phys.* **11**, 2475 (1981)
- [27] A.X. Gray, C. Papp, S. Ueda, B. Balke, Y. Yamashita, L. Plucinski, J. Minár, J. Braun, E.R. Ylvisaker, C.M. Schneider, W.E. Pickett, H. Ebert, K. Kobayashi, and C.S. Fadley, *Nature Materials* **10**, 759 (2011)
- [28] C. Papp, L. Plucinski, J. Minár, J. Braun, H. Ebert, C.M. Schneider, and C.S. Fadley, *Phys. Rev. B* **84**, 045433 (2011)
- [29] A.X. Gray, J. Minár, S. Ueda, P.R. Stone, Y. Yamashita, J. Fujii, J. Braun, L. Plucinski, C.M. Schneider, G. Panaccione, H. Ebert, O.D. Dubon, K. Kobayashi, and C.S. Fadley, *Nature Materials* **11**, 957 (2012)
- [30] J. Fujii, B.R. Salles, M. Sperl, S. Ueda, M. Kobata, K. Kobayashi, Y. Yamashita, P. Torelli, M. Utz, C.S. Fadley, A.X. Gray, J. Braun, H. Ebert, I. Di Marco, O. Eriksson, P. Thunström, G.H. Fecher, H. Stryhanyuk, E. Ikenaga, J. Minár, C.H. Back, G. van der Laan, and G. Panaccione, *Phys. Rev. Lett.* **111**, 097201 (2013)
- [31] J. Minár, J. Braun, and H. Ebert, *J. Electron. Spectrosc. Relat. Phenom.* **189**, 129 (2013)
- [32] J. Minár, J. Braun, and H. Ebert, *J. Electron. Spectrosc. Relat. Phenom.* **190**, 159 (2013)
- [33] A.X. Gray, J. Minár, L. Plucinski, M. Huijben, A. Bostwick, E. Rotenberg, S. Yang, J. Braun, A. Winkelmann, G. Conti, D. Eiteneer, A. Rattanachata, A.A. Greer, J. Ciston, C. Ophus, G. Rijnders, D.H.A. Blank, D. Doennig, R. Pentcheva, J.B. Kortright, C.M. Schneider, H. Ebert, and C.S. Fadley, *Europhys. Lett.* **104**, 17004 (2013)
- [34] J. Braun, K. Miyamoto, A. Kimura, T. Okuda, M. Donath, H. Ebert, and J. Minár, *New J. Phys.* **16**, 015005 (2014)
- [35] J. Braun, J. Minár, S. Mankovsky, V.N. Strocov, N.B. Brookes, L. Plucinski, C.M. Schneider, C.S. Fadley, and H. Ebert, *Phys. Rev. B* **88**, 205409 (2013)
- [36] J. Braun, J. Minár, F. Matthes, C.M. Schneider, and H. Ebert, *Phys. Rev. B* **82**, 024411 (2010)
- [37] J. Minár, L. Chioncel, A. Perlov, H. Ebert, M.I. Katsnelson, and A.I. Lichtenstein, *Phys. Rev. B* **72**, 045125 (2005)
- [38] J. Braun, J. Minár, H. Ebert, M.I. Katsnelson, and A.I. Lichtenstein, *Phys. Rev. Lett.* **97**, 227601 (2006)

- [39] M. Pickel, A.B. Schmidt, F. Giesen, J. Braun, J. Minár, H. Ebert, M. Donath, and M. Weinelt, *Phys. Rev. Lett.* **101**, 066402 (2008)
- [40] J. Sánchez-Barriga, J. Fink, V. Boni, I. Di Marco, J. Braun, J. Minár, A. Varykhalov, O. Rader, V. Bellini, F. Manghi, H. Ebert, M.I. Katsnelson, A.I. Lichtenstein, O. Eriksson, W. Eberhardt, and H.A. Dürr, *Phys. Rev. Lett.* **103**, 267203 (2009)
- [41] J. Braun, J. Minár, H. Ebert, A. Chainani, J. Miyawaki, Y. Takata, M. Taguchi, M. Oura, and S. Shin, *Phys. Rev. B* **85**, 165105 (2012)
- [42] J. Sánchez-Barriga, J. Braun, J. Minár, I. Di Marco, A. Varykhalov, O. Rader, V. Boni, V. Bellini, F. Manghi, H. Ebert, M.I. Katsnelson, A.I. Lichtenstein, O. Eriksson, W. Eberhardt, H.A. Dürr, and J. Fink, *Phys. Rev. B* **85**, 205109 (2012)
- [43] J. Minár, *J. Phys.: Condens. Matter* **23**, 253201 (2011)
- [44] H. Ebert, D. Ködderitzsch, and J. Minár, *Rep. Prog. Phys.* **74**, 096501 (2011)
- [45] J.S. Faulkner and G.M. Stocks, *Phys. Rev. B* **21**, 3222 (1980)
- [46] G. Kotliar, S.Y. Savrasov, K. Haule, V.S. Oudovenko, O. Parcollet, and C.A. Marianetti, *Rev. Mod. Phys.* **78**, 865 (2006)
- [47] K. Held, *Adv. Phys.* **56**, 829 (2007)
- [48] S.Y. Savrasov and G. Kotliar, *Phys. Rev. B* **69**, 245101 (2004)
- [49] P. Strange, H. Ebert, J.B. Staunton, and B.L. Gyorffy, *J. Phys.: Condens. Matter* **1**, 2959 (1989)
- [50] A.H. MacDonald and S.H. Vosko, *J. Phys. C: Solid State Phys.* **12**, 2977 (1979)
- [51] R.M. Dreizler and E.K.U. Gross: *Density Functional Theory* (Springer-Verlag, Heidelberg, 1990)
- [52] H. Ebert, S. Bornemann, J. Braun, D. Ködderitzsch, S. Lowitzer, S. Mankovsky, J. Minár, M. Offenberger, S. Polesya, , and V. Popescu: *Recent Developments in KKR Theory* [http://www.psi-k.org/newsletters/News\\_97/Highlight\\_97.pdf](http://www.psi-k.org/newsletters/News_97/Highlight_97.pdf)
- [53] A. Gonis and W.H. Butler: *Multiple scattering in solids*
- [54] E. Tamura, *Phys. Rev. B* **45**, 3271 (1992)
- [55] E.N. Economou: *Green's Functions in Quantum Physics*, Springer Series in Solid-state Sciences, Vol. 7 (Springer, Berlin, 1990)
- [56] R. Zeller, J. Deutz, and P.H. Dederichs, *Solid State Commun.* **44**, 993 (1982)

- [57] L.V. Pourovskii, M.I. Katsnelson, and A.I. Lichtenstein, *Phys. Rev. B* **72**, 115106 (2005)
- [58] S. Chadov: *Application of Many-Body Perturbation Theory to the Description of Correlated Metals*
- [59] S. Chadov, J. Minár, M.I. Katsnelson, H. Ebert, D. Ködderitzsch, and A.I. Lichtenstein, *Europhys. Lett.* **82**, 37001 (2008)
- [60] J. Sánchez-Barriga, J. Minár, J. Braun, A. Varykhalov, V. Boni, I. Di Marco, O. Rader, V. Bellini, F. Manghi, H. Ebert, M.I. Katsnelson, A.I. Lichtenstein, O. Eriksson, W. Eberhardt, H.A. Dürr, and J. Fink, *Phys. Rev. B* **82**, 104414 (2010)
- [61] S. Biermann, F. Aryasetiawan, and A. Georges, *Phys. Rev. Lett.* **90**, 086402 (2003)
- [62] P. Soven, *Phys. Rev.* **156**, 809 (1967)
- [63] J.S. Faulkner, *Prog. Mater. Sci.* **27**, 1 (1982)
- [64] V. Drchal, V. Janiš, and J. Kudrnovský, *Phys. Rev. B* **60**, 15664 (1999)
- [65] I. Turek, V. Drchal, J. Kudrnovský, M. Sob, and P. Weinberger: *Electronic structure of disordered alloys, surfaces and interfaces* (Kluwer Academic Publ., Boston, 1997)
- [66] O. Šipr, J. Minár, S. Mankovsky, and H. Ebert, *Phys. Rev. B* **78**, 144403 (2008)
- [67] K. Held, I.A. Nekrasov, G. Keller, V. Eyert, N. Blümer, A.K. McMahan, R.T. Scalettar, T. Pruschke, V.I. Anisimov, and D. Vollhardt, *phys. stat. sol. (b)* **243**, 2599 (2006)
- [68] F. Manghi, V. Bellini, J. Osterwalder, T.J. Kreutz, P. Aebi, and C. Arcangeli, *Phys. Rev. B* **59**, R10409 (1999)
- [69] K. Kambe, *Z. Naturf.* **22a**, 322 (1967)
- [70] J.M. MacLaren, S. Crampin, D.D. Vvedensky, and J.B. Pendry, *Phys. Rev. B* **40**, 12164 (1989)
- [71] G. Malmström and J. Rundgren, *Comp. Phys. Commun.* **19**, 263 (1980)
- [72] T. Fujikawa and H. Arai, *J. Elec. Spec. Rel. Phenom.* **123**, 19 (2002)
- [73] T. Fujikawa and H. Arai, *J. Electron. Spectrosc. Relat. Phenom.* **174**, 85 (2009)
- [74] G. Borstel, *Appl. Physics A* **38**, 193 (1985)
- [75] J. Braun: *New developments in UP- and XP-spectroscopy from ferromagnetic materials, in Band-Ferromagnetism* (Springer, Berlin, 2001), p. 341
- [76] G. Hilgers, M. Potthoff, N. Müller, U. Heinzmann, L. Hainert, J. Braun, and G. Borstel, *Phys. Rev. B* **52**, 14859 (1995)

- [77] R. Feder, *J. Phys. C: Solid State Phys.* **14**, 2049 (1981)
- [78] M. Potthoff, J. Lachnitt, W. Nolting, and J. Braun, *phys. stat. sol. (b)* **203**, 441 (1997)
- [79] H. Ebert, *Rep. Prog. Phys.* **59**, 1665 (1996)
- [80] U. Fano, *Phys. Rev.* **178**, 131 (1969)
- [81] J. Minár, H. Ebert, C. De Nadaï, N.B. Brookes, F. Venturini, G. Ghiringhelli, L. Chioncel, M.I. Katsnelson, and A.I. Lichtenstein, *Phys. Rev. Lett.* **95**, 166401 (2005)
- [82] J. Minár, H. Ebert, G. Ghiringhelli, O. Tjernberg, N.B. Brookes, and L.H. Tjeng, *Phys. Rev. B* **63**, 144421 (2001)
- [83] C. De Nadaï, J. Minár, H. Ebert, G. Ghiringhelli, A. Tagliaferri, and N.B. Brookes, *Phys. Rev. B* **70**, 134409 (2004)
- [84] S. Hüfner and G.K. Wertheim, *Phys. Letters A* **51A**, 299 (1975)
- [85] C. Guillot, Y. Ballu, J. Paigné, J. Lecante, K.P. Jain, P. Thiry, R. Pinchaux, Y. Pétrouff, and L.M. Falicov, *Phys. Rev. Lett.* **39**, 1632 (1977)
- [86] A. Kakizaki, K. Ono, K. Tanaka, K. Shimada, and T. Sendohda, *Phys. Rev. B* **55**, 6678 (1997)
- [87] K.N. Altmann, D.Y. Petrovykh, G.J. Mankey, N. Shannon, N. Gilman, M. Hochstrasser, R.F. Willis, and F.J. Himpsel, *Phys. Rev. B* **61**, 15661 (2000)
- [88] J. Osterwalder, *J. Elec. Spec. Rel. Phenom.* **117-118**, 71 (2001)
- [89] N. Kamakura, Y. Takata, T. Tokushima, Y. Harada, A. Chainani, K. Kobayashi, and S. Shin, *Phys. Rev. B* **74**, 045127 (2006).
- [90] O. Karis, S. Svensson, J. Ruzs, J. Oppeneer, M. Gorgoi, F. Schäfers, W. Braun, W. Eberhardt, M. Mårtensson, *Phys. Rev. B* **78**, 233105 (2008)
- [91] A. Liebsch, *Phys. Rev. Lett.* **43**, 1431 (1979)
- [92] A. Liebsch, *Phys. Rev. B* **23**, 5203 (1981)
- [93] O. Miura and T. Fujiwara, *Phys. Rev. B* **77**, 195124 (2008)
- [94] D.E. Eastman, F.J. Himpsel, and J.A. Knapp, *Phys. Rev. Lett.* **40**, 1514 (1978)
- [95] F.J. Himpsel, J.A. Knapp, and D.E. Eastman, *Phys. Rev. B* **19**, 2919 (1979)
- [96] W. Eberhardt and E.W. Plummer, *Phys. Rev. B* **21**, 3245 (1980)
- [97] C.S. Wand and J. Callaway, *Phys. Rev. B* **15**, 298 (1977)

- [98] J. Kanski, P.O. Nilsson, and C.G. Larsson, *Solid State Commun.* **35**, 397 (1980)
- [99] Y. Sakisaka, T. Kommeda, M. Onchi, H. Kato, S. Masuda, and K. Yagi, *Phys. Rev. B* **36**, 6383 (1987)
- [100] T. Kinoshita, T. Ikoma, A. Kakizaki, T. Ishii, J. Fujii, H. Fukutani, K. Shimada, A. Fujimori, T. Okane, and S. Sato, *Phys. Rev. B* **47**, 6787 (1993)
- [101] N. Nakajima, S. Hatta, J. Odagiri, H. Kato, and Y. Sakisaka, *Phys. Rev. B* **70**, 233103, (2004)
- [102] A.I. Lichtenstein, M.I. Katsnelson, and G. Kotliar, *Phys. Rev. Lett.* **87**, 067205 (2001)
- [103] W. Eberhardt, E.W. Plummer, K. Horn, and J. Erskine, *Phys. Rev. Lett.* **45**, 273 (1980)
- [104] C. Calandra and F. Manghi, *Phys. Rev. B* **50**, 2061 (1994)
- [105] M.M. Steiner, R.C. Albers, and L.J. Sham, *Phys. Rev. B* **45**, 13272 (1992)
- [106] M. Cococcioni and S. de Gironcoli, *Phys. Rev. B* **71**, 035105 (2005)
- [107] T. Allmers, M. Donath, J. Braun, J. Minár, and H. Ebert, *Phys. Rev. B* **84**, 245426 (2011)
- [108] S. Tanuma, C.J. Powell, and D.R. Penn, *Surface and Interface Analysis* **43**, 689 (2011)
- [109] Z. Hussain, C.S. Fadley, S. Kono, and L.F. Wagner, *Phys. Rev. B* **22**, 3750 (1980)
- [110] E.H. Sondheimer, *Adv. Phys.* **50**, 499 (2001)
- [111] A. Sekiyama and S. Suga, *J. Electron Spectrosc. Relat. Phenom.* **137**, 681 (2004)
- [112] A. Yamasaki, A. Sekiyama, S. Imada, M. Tsunekawa, A. Higashiya, A. Shigemoto, S. Suga, *Nucl. Instr. and Meth. Phys. Res. A* **547**, 136 (2005)
- [113] T. Yokoya, T. Nakamura, T. Matsushita, T. Muro, Y. Takano, M. Nagao, T. Takenouchi, H. Kawarada, and T. Oguchi, *Nature* **438**, 647 (2005)
- [114] M. Yano, A. Sekiyama, H. Fujiwara, T. Saita, S. Imada, T. Muro, Y. Onuki, and S. Suga, *Phys. Rev. Lett.* **98**, 036405 (2007)
- [115] L. Plucinski, J. Minár, B.C. Sell, J. Braun, H. Ebert, C.M. Schneider, and C.S. Fadley, *Phys. Rev. B* **78**, 035108 (2008)
- [116] F. Venturini, J. Minár, J. Braun, H. Ebert, and N.B. Brookes, *Phys. Rev. B* **77**, 045126 (2008)
- [117] S. Suga and A. Sekiyama, *J. Electron Spectrosc. Relat. Phenom.* **181**, 48 (2010)
- [118] C.S. Fadley, *Synchrotron Radiation News* **25**, 26 (2012)

- 
- [119] V.N. Strocov, M. Shi, M. Kobayashi, C. Monney, X. Wang, J. Krempasky, T. Schmitt, L. Patthey, H. Berger, and P. Blaha, *Phys. Rev. Lett.* **109**, 086401 (2012)
- [120] J. Minár, J. Braun, S. Mankovsky and H. Ebert, *J. Electron Spectrosc. Relat. Phenom.* **184**, 91 (2011)
- [121] M. Kobayashi, I. Muneta, Y. Takeda, Y. Harada, A. Fujimori, J. Krempasky, T. Schmitt, S. Ohya, M. Tanaka, M. Oshima, and V.N. Strocov, arxiv.1302.0063v1
- [122] R. Courts, V. Bachelier, and S. Hüfner, *Solid State Commun.* **38**, 887 (1981)
- [123] P.S. Wehner, R.S. Williams, S.D. Kevan, D. Denley, and D.A. Shirley, *Phys. Rev. B* **19**, 6164 (1979)
- [124] J.G. Nelson, S. Kim, W.J. Gignac, R.S. Williams, J.G. Tobin, S.W. Robey, and D.A. Shirley, *Phys. Rev. B* **32**, 3465 (1985)
- [125] N.J. Shevchik, *Phys. Rev. B* **16**, 3428 (1977)
- [126] C.G. Larsson and J.B. Pendry, *J. Phys. C: Solid State Phys.* **14**, 3089 (1981)
- [127] M.A.V. Alvarez, H. Ascolani, and G. Zampieri, *Phys. Rev. B* **54**, 14703 (1996)